Dissertations in Forestry and Natural Sciences

UNIVERSITY OF
EASTERN FINLAND

OLLI NYKÄNEN

MAGNETIC RESONANCE IMAGING OF THE OSTEOCHONDRAL UNIT: STUDIES USING QUANTITATIVE SUSCEPTIBILITY MAPPING AND SWEEP IMAGING WITH FOURIER TRANSFORM

Olli Nykänen

MAGNETIC RESONANCE IMAGING OF THE OSTEOCHONDRAL UNIT: STUDIES USING QUANTITATIVE SUSCEPTIBILITY MAPPING AND SWEEP IMAGING WITH FOURIER TRANSFORM

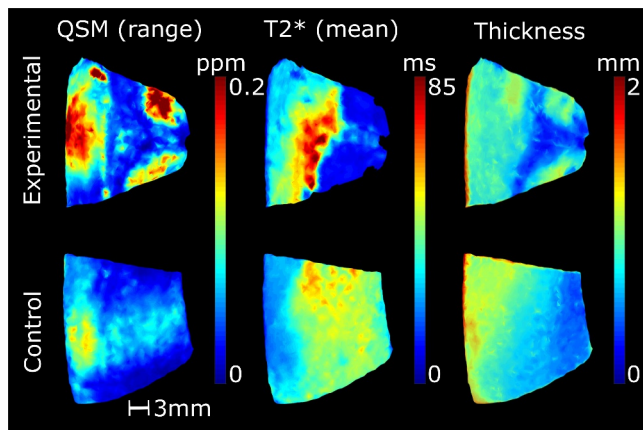

To be presented by the permission of the Faculty of Science and Forestry for public examination in the Auditorium SN200 in Snellmania building at the University of Eastern Finland, Kuopio, on September, 4, 2020, at 16:30 o'clock.

Author's address: University of Eastern Finland
Department of Applied Physics
FI-70211 Kuopio
FINLAND
email: olli.nykanen@uef.fi

Supervisors: Academy Research Fellow Mikko Nissi
University of Eastern Finland
Department of Applied Physics
FI-70211 Kuopio
FINLAND
email: mikko.nissi@uef.fi

Professor Juha Töyräs
University of Queensland
School of Information Technology
and Electrical Engineering
Brisbane
AUSTRALIA
email: j.toyras@uq.edu.au

Professor Ville Kolehmainen
University of Eastern Finland
Department of Applied Physics
FI-70211 Kuopio
FINLAND
email: ville.kolehmainen@uef.fi

Reviewers: Professor Jiang Du
University of California San Diego
School of Health Sciences
San Diego
UNITED STATES OF AMERICA
email: jiangdu@ucsd.edu

Associate Professor Simon Robinson
Medizinische Universität Wien
Department of Biomedical Imaging
and Image-guided Therapy
Wien
AUSTRIA
email: simon.robinson@meduniwien.ac.at

Opponent: Associate Professor Chunlei Liu
University of California Berkeley
School of Electrical Engineering
and Computer Sciences
Berkeley
UNITED STATES OF AMERICA
email: chunlei.liu@eecs.berkeley.edu

ABSTRACT

Osteoarthritis (OA) is a common disease that causes degeneration of articular cartilage and other joint tissues. The progression of OA can lead to severe pain and immobility. Unfortunately, clinical imaging techniques are more suited to diagnosing the late stages of the disease rather than detecting the early signs of degeneration. Therefore, new non-invasive imaging methods are urgently needed that could assess the compositional changes related to incipient OA in joint connective tissues.

Quantitative MRI parameters, such as relaxation time constants or diffusion, are among the most promising methods for the non-invasive assessment of early changes evoked by OA. However, many of these quantitative parameters have significant shortcomings, such as long imaging times, very low sensitivity or requirement of special hardware, which mean that they are inapplicable for clinical imaging. Furthermore, a significant issue limiting the use of quantitative MRI for OA diagnostics is the rapid transversal relaxation often observed in the musculoskeletal tissues, reducing the signal available from these tissues. This issue can be overcome by applying the ultra-short or zero echo time methods. Interestingly, when using these methods, a previously unseen hyperintense signal has been observed at the osteochondral junction. However, the exact origin of this signal has not been comprehensively studied, and even its location in the osteochondral unit has remained debatable as both deep uncalcified cartilage and calcified cartilage have been proposed.

The hypotheses of this thesis were that quantitative susceptibility mapping (QSM) could overcome at least most of the problems regarding quantitative MRI assessment of articular cartilage and more specifically, that it would be sensitive to the changes in the properties of the extracellular matrix of articular cartilage. Regarding the hyperintense signal at the osteochondral junction, it was hypothesized that this signal is located in the deep uncalcified cartilage instead of the calcified cartilage. Moreover, it was hypothesized that the hyperintense signal would be in part generated by and dependent on the susceptibility differences between the uncalcified and calcified cartilage.

All experiments were performed by imaging ex vivo osteochondral samples of animal and human origin in a preclinical 9.4T MRI scanner. When evaluating QSM in the assessment of articular cartilage, it was compared to T_2^* relaxation time mapping and also correlated with reference parameters, such as biomechanical properties or collagen network organization in articular cartilage. Furthermore, the poten-

tial added value by combining the QS- and T_2^* mapping for diagnosis of cartilage degeneration was studied. To localize the hyperintense signal at the osteochondral junction, co-registration was performed between SWIFT-MRI, high-resolution μCT and the histological images. T_1 relaxation time mapping and variable bandwidth SWIFT imaging were utilized to reveal the potential causes of the hyperintense signal.

The results of the thesis indicate that native QSM has a limited ability to detect cartilage degeneration and seems to lack sensitivity compared to the T_2^* relaxation time mapping. However, the combination of the information obtained with both methods (available from the same measurement) improves the results over those gathered by using either of the methods individually.

The results using SWIFT-MRI indicated that the hyperintense signal at the osteochondral junction is completely observed in the deepest parts of non-calcified articular cartilage instead of the calcified cartilage or subchondral bone. It was observed that the region of the hyperintense signal in the deep layer had a much shorter T_1 relaxation time than the superficial cartilage. Moreover, the multiple bandwidths test demonstrated that the hyperintense signal was blurred at lower receiver bandwidths. These results indicate that the hyperintense signal is at least partially caused by the fast T_1 relaxation and that the susceptibility differences between the uncalcified and calcified cartilage have a role in generating the signal. As the susceptibility effects are a potential cause of the hyperintense signal, the combination of SWIFT and QSM could potentially be used to clarify this signal better.

National Library of Medicine Classification: WE 300, WE 348, WN 185

Medical Subject Headings: Cartilage, Articular; Osteoarthritis/diagnosis; Extracellular Matrix; Diagnostic Imaging; Magnetic Resonance Imaging
Yleinen suomalainen ontologia: nivelrusto; nivelrikko; soluväliaine; kuvantaminen; magneettikuvaus

ACKNOWLEDGEMENTS

never have been possible.

Kuopio, August 9th, 2020
Olli Nykänen

LIST OF PUBLICATIONS

This thesis consists of the present review of the author's work in the field of magnetic resonance imaging of articular cartilage and the following selection of the author's publications:

I Nykänen, Olli; Rieppo, Lassi; Töyräs, Juha; Kolehmainen, Ville; Saarakkala, Simo; Shmueli, Karin; Nissi Mikko J. "Quantitative susceptibility mapping of articular cartilage: Ex vivo findings at multiple orientations and following different degradation treatments." Magnetic resonance in medicine 80.6 (2018): 2702-2716.

II Nykänen, Olli; Sarin, Jaakko K.; Ketola, Juuso H.; Leskinen, Henri P.P.; te Moller, Nikae C.R.; Tiitu, Virpi; Mancini, Irina A.D.; Visser, Jetze; Brommer, Harold; van Weeren, P. Rene; Malda, Jos; Töyräs, Juha; Nissi, Mikko J. "T_2^* and quantitative susceptibility mapping in an equine model of post-traumatic osteoarthritis: assessment of mechanical and structural properties of articular cartilage." Osteoarthritis and cartilage 27.10 (2019): 1481-1490.

III Nykänen, Olli; Leskinen, Henri P.P.; Finnilä, Mikko A.J.; Karhula, Sakari S.; Turunen, Mikael J.; Töyräs, Juha; Saarakkala, Simo; Nissi, Mikko J. . "The bright ultra-short echo time SWIFT MRI signal at the osteochondral junction is not located in the calcified cartilage" Journal of Orthopaedic Research, Under review

Throughout the overview, these papers will be referred to by Roman numerals.

AUTHOR'S CONTRIBUTION

The publications included in this dissertation are original research papers on magnetic resonance imaging of articular cartilage.

I The author conducted all MRI measurements and performed sample preparations and most of the data-analysis. The author also designed the simulations performed in the study. The author was the main author of the manuscript.

II The author designed the MRI measurements and performed most of the data-analysis and was the main contributor in writing the manuscript.

III The author performed and partially designed the MRI measurements and also performed most of the analysis in the manuscript and was the main author of the manuscript.

TABLE OF CONTENTS

1 Introduction

Articular cartilage is a tissue covering the ends of articulating bones. Together with the synovial fluid, it provides nearly frictionless motion of joints [1]. Furthermore, it also contributes to the transmission of loads in the joint [2]. However, as articular cartilage has no vasculature and a relatively low number of cells, it has only a limited ability to recover from damage [2].

Degenerative diseases, such as osteoarthritis (OA), can lead to a permanent destruction of articular cartilage and eventually to pain of the diseased joint, causing immobility. Nowadays OA is a common disease in Western societies, affecting especially the elderly population; for example, knee OA affects over 10% of the population older than 60 [3–5]. Since OA may lead to disability and require surgical operations, such as total knee arthroplasty, as a treatment, it poses a major burden on the healthcare budget; for example in Finland, the annual costs of OA are around one billion (1 000 000 000) euros [6]. Despite the high socio-economic impact of the disease and the significant scientific effort to find ways to prevent the disease, there are no effective disease-modifying drugs for OA [7]. The development of disease-modifying drugs would require the ability to detect and follow-up even the smallest of changes in the properties of cartilage. In addition, because articular cartilage has a low ability to regenerate, the detection of changes caused by OA, other diseases or trauma should be detected before the damage has progressed to a terminal stage [8]. However, current clinical methods such as estimating the joint space narrowing from plain radiographs, qualitative magnetic resonance imaging and arthroscopy are qualitative in nature (arthroscopy is also invasive), which hampers their potential to act as early biomarkers for OA [9].

Magnetic resonance imaging (MRI) offers the unique ability to image different properties of tissues simply by modifying the applied imaging sequence, without the need to alter the hardware or inject contrast agents into the patients. Many quantitative MRI parameters have been studied for imaging of articular cartilage, but to date, they have suffered from long scan times, limiting them to 2-D imaging or low resolution (gagCEST) [10, 11], from hardware dependence (relaxation times) [12], or the need to administer contrast agents or the availability of special hardware (dGEMRIC and sodium imaging respectively) [11–13].

In this thesis, the potential of quantitative susceptibility mapping (QSM) [14] and ultra-short echo time imaging using the SWIFT sequence [15] was evaluated in the imaging of articular cartilage. QSM was studied, since it overcomes many of the issues limiting the use of quantitative MRI in cartilage imaging. Ultra-short echo time methods, on the other hand, have already demonstrated their potential in musculoskeletal imaging, since they are able to provide signals from tissues that are usually invisible in MRI [15–17].

While studies **I** and **II** of the thesis revealed that QSM is still far from ready to be utilized in clinical imaging of articular cartilage, they hinted that it may have potential when used properly. In study **III**, SWIFT imaging revealed interesting and new information about the MRI detectable signals in the vicinity and at the osteochondral junction, which has recently attracted interest with respect to its role

1

in the initiation and progression OA. Thus, the findings in this thesis provide novel information and hint at potentially important developments for OA diagnosis in the future.

2   Articular Cartilage

The ends of articulating bones are covered by articular cartilage, which together with the synovial fluid, allows nearly frictionless motion of joints [1]. To some extent, articular cartilage functions as a shock absorber during motion as it distributes loads evenly to the underlying bones [2]. Articular cartilage consists of interstitial water and extracellular matrix and chondrocytes [2]. The extracellular matrix is mostly composed of a collagen fiber network and proteoglycan macromolecules [2]. The number of cells in mature cartilage is relatively low, constituting only around 2% of the total volume of articular cartilage [2, 18]. Both low friction and the high shock absorbing and weight bearing abilities of articular cartilage are provided by its complex structure [2]. Articular cartilage is attached to the bone via the calcified cartilage layer at the osteochondral junction (Figure 2.1) [19].
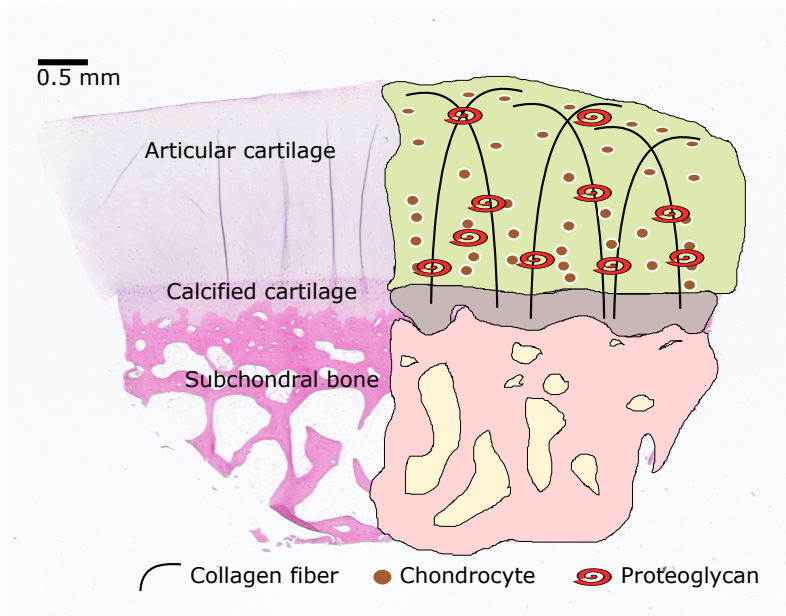
Figure 2.1: Structure of the osteochondral unit as seen in a hematoxylin and eosin (H&E) stained histological slice and a schematic drawing depicting the main structures and constituents of articular cartilage. Non-calcified articular cartilage is separated from the calcified cartilage by the tidemark. The border between the calcified cartilage and subchondral bone is called the cement line.

2.1   COLLAGEN NETWORK

The function of the collagen network in cartilage is to provide structure, which holds all the other constituents of cartilage together. Collagen in articular cartilage

accounts for around 20% of the tissue wet weight (about 60% of dry weight), and the relative amount of collagen increases as one moves towards the osteochondral junction [2, 20, 21]. The collagen of articular cartilage is mainly type II collagen, but also other collagen types (*e.g.* III, VI, IX and XI) are present [2]. In articular cartilage, collagen forms fibers that are organized into a network that confers cartilage with its tensile strength and provides a frame into which other constituents of articular cartilage can bind [2, 20]. The collagen fibers consist of fibrils that are formed by multiple collagen molecules attached to each other [22]. Moreover, collagen molecules consist of three left-handed helices formed of type II collagen [22]. The other types of collagen in articular cartilage help to form and stabilize the collagen fibrils [2]. Articular cartilage can be divided into three zones based on the orientation and anisotropy of the collagen fibers [2, 23]. In the superficial zone, collagen fibers are oriented in parallel to the surface of the articular cartilage; in the transitional zone, collagen fibers are bent away from a parallel orientation with respect to the surface towards an orientation that is perpendicular to the surface and in the radial zone, the fibers are almost perpendicular to the cartilage-bone interface (Figure 2.2) [2, 23]. The collagen fibers of the radial zone are attached to the subchondral bone via calcified cartilage [2].

2.2 PROTEOGLYCANS

Proteoglycans are the other main constituent of the extracellular matrix along with the collagen network. Proteoglycans make up approximately 5% of the wet weight of articular cartilage (30% of the dry weight) [2, 20]. Proteoglycans are formed by glycosaminoglycan (GAG) molecules that are attached to a core protein [2]. GAGs are composed of long chains of disaccharide units, which in turn contain an amino sugar [2]. The disaccharide units contain negatively charged sulphate or carboxylate groups, making GAGs negatively charged. The negative charge of GAGs attracts cations and thus water into cartilage [20]. The proteoglycans in cartilage tend to form large aggrecans, having a high charge density leading to a swelling of the articular cartilage [20]. This swelling is restricted by the collagen network of articular cartilage and eventually an equilibrium state is reached between the tensile forces in the collagen network and the swelling pressure created by the proteoglycans [24]. Proteoglycans restrict the fluid flow when pressure is applied to articular cartilage and also give cartilage its ability to recover after the pressure is relieved [24]. The proteoglycan concentration in the articular cartilage increases towards the osteochondral junction (Figure 2.2) [2].

2.3 CHONDROCYTES

Chondrocytes are the only cell-type that exist in articular cartilage and they are surrounded by the extracellular matrix of the articular cartilage [2]. Chondrocytes synthesize collagen and proteoglycans and have an ability to react to changes in their environment [2]. Thus, chondrocytes are responsible for producing and maintaining the complex structure of articular cartilage [2]. The chondrocytes are most active during the growth of cartilage; in mature articular cartilage, their activity is decreased [2]. The shape of the chondrocyte cells depends on their location in articular cartilage; the superficial cells have an oval shape whereas in the radial zone, the chondrocytes are round [25]. Although chondrocytes have an ability to produce

the constituents of the extracellular matrix of articular cartilage, they are not able to repair severe damage [20]. In mature cartilage, chondrocytes receive nutrients only from the synovial fluid by means of diffusion [2]. The numbers of chondrocytes are highest in the radial zone of articular cartilage (Figure 2.2).

2.4 INTERSTITIAL FLUID

The amount of interstitial fluid is around 60-80% of the wet weight of articular cartilage [20]. Most of the interstitial fluid in articular cartilage is associated with the proteoglycans, while one third of the water is bound to collagen fibers and a small amount is located in the chondrocytes [26]. Although water in articular cartilage is mostly associated with either the proteoglycan or collagen macromolecules, it is not trapped but instead exchangeable [27]. Together with the synovial fluid, interstitial fluid is responsible for providing nutrients and oxygen to the chondrocytes, since mature articular cartilage is a completely avascular tissue [2]. The water content of articular cartilage is controlled by the proteoglycan concentration and the organization of the collagen network [26]. The water content of articular cartilage is highest in the superficial zone of articular cartilage and decreases towards the osteochondral junction (OCJ) (Figure 2.2) [2].
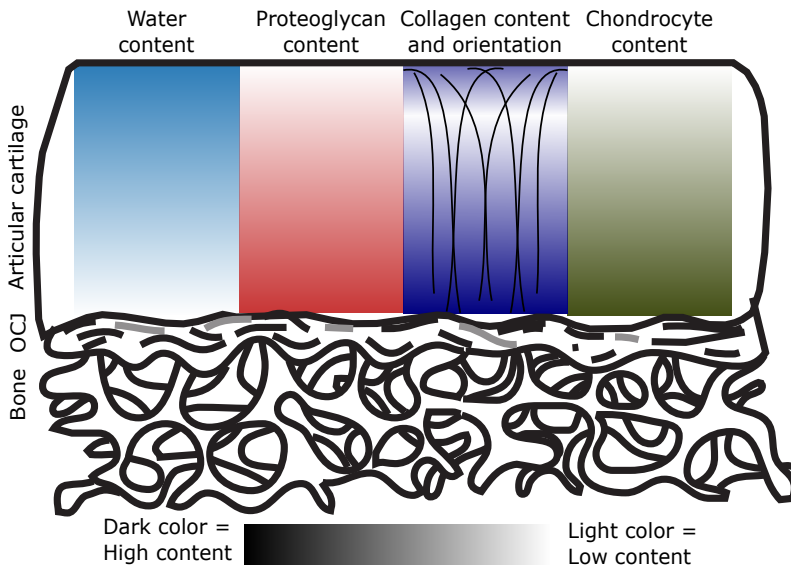
Figure 2.2: The constituents of articular cartilage and their concentrations in the different layers of articular cartilage. Darker color indicates a higher concentration of each constituent. Black lines in the collagen column depict the collagen fibers and their orientation.

2.5 OSTEOCHONDRAL JUNCTION

The osteochondral junction (OCJ) is the area at the border of articular cartilage and subchondral bone, where the collagen fibers of articular cartilage are attached into

subchondral bone via the tidemark and calcified cartilage [2]. The calcified cartilage is formed as calcification extends from the subchondral bone plate to the deepest parts of articular cartilage, providing a very strong attachment and a transitional zone between the collagen network of articular cartilage and the subchondral bone [19, 28, 29]. The collagen network and composition of calcified cartilage are somewhat similar to the deepest parts of articular cartilage and differ greatly from the structure of bone (Figure 2.3), *i.e.* calcified cartilage is literally calcified, but not ossified radial cartilage [19, 29]. The borderline between the calcified cartilage and articular cartilage is called the tidemark [29]. The composition and structure of the tidemark is not yet completely understood [19]. During cartilage growth, cartilage obtains nutrients from the vasculature that comes to the cartilage through the osteochondral junction, but towards the end of the growth, this vasculature vanishes [19], meaning that superficial cartilage has to acquire its nutrition from the synovial fluid [2]. However, the deepest parts of cartilage (*i.e.* the osteochondral junction) obtain their nutrients via the subchondral plate [29]. The border between the calcified cartilage and subchondral bone is called the cement line [19, 29]
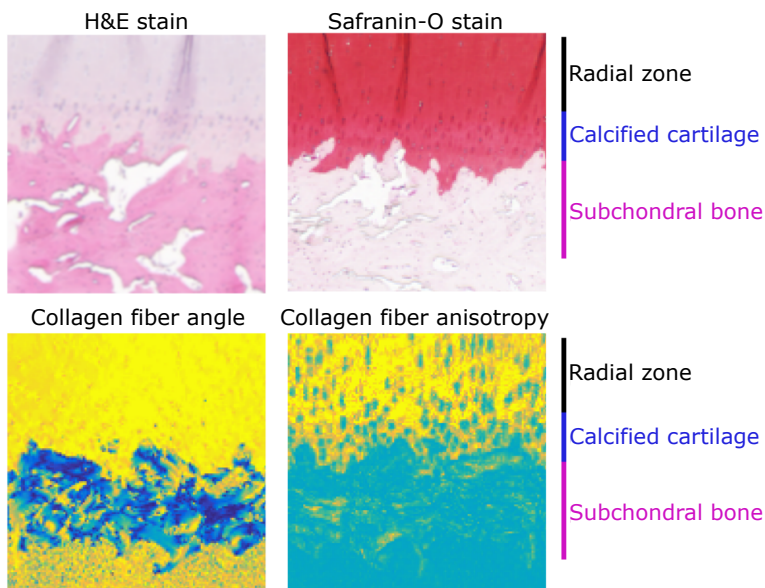
Figure 2.3: Light microscope images of the osteochondral junction. The first row shows ordinary light microscope images of H&E and Safranin-O stained histological sections and the bottom row displays the collagen fiber and anisotropy from polarized light microscopy. It can be seen that the calcified cartilage resembles radial articular cartilage (more than subchondral bone) in each case. The resemblance is so clear that with many histological methods, it is difficult to make a distinction between the calcified and non-calcified cartilage.

2.6   OSTEOARTHRITIS

Osteoarthritis is a degenerative disease of joint tissues, involving articular cartilage. Osteoarthritis is common, especially in the elderly population and it causes severe pain and ultimately in the immobility of patient with the progression of the disease. Traditionally, OA was believed to be a disease of articular cartilage, but nowadays it is known to affect all joint tissues [29].

Osteoarthritis is associated with a loss of proteoglycans, changes in the water content, disruption of the collagen network and changes in the osteochondral junction and subchondral bone. These changes include bone remodelling, sclerosis, re-vascularization of the osteochondral junction and deep cartilage, and tidemark duplication (Figure 2.4) [4,5,30–32].
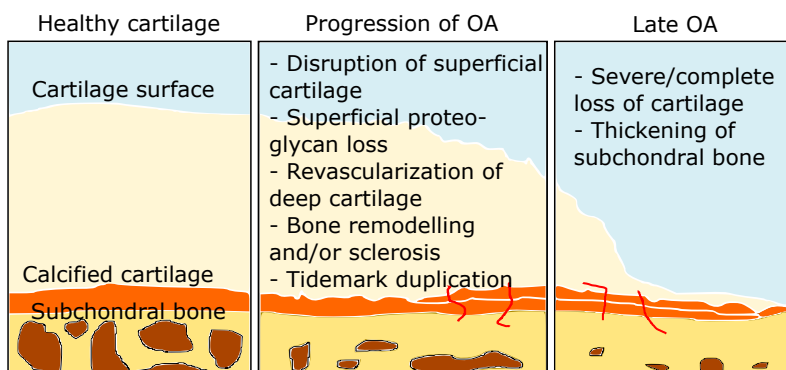
Figure 2.4: Progression of osteoarthritis in the osteochondral unit. At the beginning of the disease, the cartilage surface starts to become disrupted and also the changes at the osteochondral junction begin to progress. As the disease progresses, the cartilage becomes thinner and subchondral bone thickens.

The changes in the cartilage-bone unit due to osteoarthritis happen gradually and it is not easy to detect the initial changes. This is complicated by the fact that articular cartilage is aneural, and thus the pain occurs only after OA has caused inflammation [4]. Most often, superficial proteoglycan loss and the fibrillation of collagen network are thought to be the first signs of OA [4]. Sclerosis of the subchondral bone may also appear during the early stages of OA [33]. During OA progression, the collagen matrix of articular cartilage is damaged and proteoglycans are lost also from the deeper parts of the tissue. Thickening of the subchondral bone and changes at the osteochondral junction also take place gradually as the OA progresses [29,34].

Although the changes to the tissues of the osteochondral unit during the progression of osteoarthritis are well known, the exact cause (or causes) that initiates osteoarthritis is currently unknown and is a topic of investigation. One special case of osteoarthritis is post-traumatic osteoarthritis, in which the OA is initiated by trauma, such as anterior cruciate ligament rupture or meniscal tear [30]. As the exact cause of OA is not well known, there are no drugs that could slow down or prevent OA, let alone heal advanced OA [7]. Since there is no disease-modifying medication for OA, early diagnosis of the disease is necessary if one wishes to initiate rehabilitative treatment early enough to affect the prognosis [8]. For example, the re-

habilitation for OA includes weight management and strengthening of muscles [35]. Importantly, the lack of an early imaging biomarker for OA has complicated the search of disease-modifying drugs for OA [9].

3 Magnetic resonance imaging

In this chapter, the foundations of magnetic resonance imaging (*i.e.* nuclear magnetic resonance (NMR)) are reviewed first, then the measurement of the NMR signal is explained and the pulse sequences used in this thesis are shortly described. At the end of the chapter, the principles and methodology of Quantitative Susceptibility Mapping (QSM) are explained. The first three subchapters are covered in greater detail in multiple textbooks, *e.g.* [36–40].

3.1 NUCLEAR MAGNETIC RESONANCE

Magnetic resonance imaging (MRI) is based on the nuclear magnetic resonance, which is caused by the spin angular momentum (spin) of the nuclei. In an external magnetic field, the spins are locked along the external field and take the superposition of the allowed quantum states, the number of which depends on the nuclei that are being imaged. Furthermore, in the external field, the spins are precessing around the axis of the main field at the Larmor frequency ω_0 (the resonance frequency of the spin system), which is defined as follows

$$\omega_0 = -\gamma \vec{B}_0, \tag{3.1}$$

where γ is the gyromagnetic ratio of the imaged nuclei and $\vec{B}_0$ is the external magnetic field.

For the most commonly imaged nucleus, hydrogen, the spin is $1/2$, which allows two states with different energy levels. In the external field, the spins will reach a thermodynamical equilibrium, where there will be slightly more spins at the lower energy state. The distribution of spins at both energy states is given by the Boltzmann distribution:

$$\frac{N_1}{N_2} = e^{(-\gamma h \vec{B}_0/2\pi)/kT}, \tag{3.2}$$

where N_i is the amount of spins at both energy states, h is Planck's constant, k is Boltzmann's constant and T is temperature. The energy difference between the states is now $\Delta E = -\gamma h \vec{B}_0/2\pi$. Since the amount of spins is different at low and high energy states, a net magnetization is formed along the main magnetic field. In MRI, the net magnetization vector is manipulated to create a signal from the region of interest.

3.2 RELAXATION

In NMR experiments (such as MRI), the measured signal is generated by disturbing the net magnetization by applying radiofrequency pulses at the Larmor frequency. More specifically, since the transverse component of the net magnetization produces a signal that is measurable by the RF-coil, the net magnetization is tilted from the axis of the main field towards transverse plane via the application of RF-pulse.

After the equilibrium is disturbed, the spin system starts to recover towards the equilibrium via different relaxation processes, namely longitudinal and transversal relaxations.

The longitudinal or T_1-relaxation (sometimes also called spin-lattice relaxation also) describes how quickly the net magnetization returns to the equilibrium state after the perturbation. T_1-relaxation is affected by the molecular motion causing fluctuations in the magnetic field that the spins experience, causing their polarization axes to wander. Thus, for example when a sample is brought into a magnetic field, the net magnetization is not instantly formed, but needs a finite time to form (Figure 3.1). T_1-relaxation is mostly affected by molecular motions nearby to the Larmor frequency of the spins.
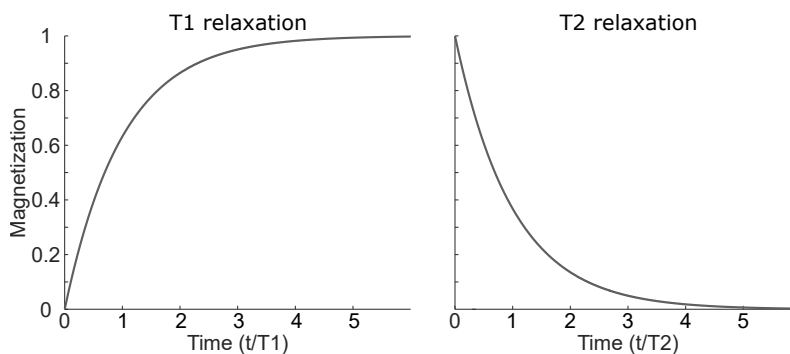
Figure 3.1: Left: magnetization along main magnetic field as a function of time after an object is brought into a magnetic field, *i.e.* T_1-relaxation. Right: transverse component of magnetization as a function of time after excitation RF-pulse, *i.e.* T_2-relaxation

As the main field is usually cylindrically symmetrical, there is no naturally occurring transverse component for net magnetization. However in MRI, the net magnetization is tilted towards the transverse plane to obtain a measurable signal. towards the transverse plane to obtain a measurable signal. Transversal or T_2-relaxation (also spin-spin relaxation) describes the decay of the transverse component of the net magnetization vector. As the net magnetization is brought to the transverse plane, it starts to precess around the longitudinal axis. During precession, the individual spins start to dephase due to fluctuations in the magnetic fields. This dephasing in turn causes an irreversible decay in the transverse magnetization. T_2-relaxation is affected by the molecular motions but in contrast to the T_1-relaxation, motions at much lower frequencies than Larmor frequency play a role in the transverse relaxation.

Both T_1-relaxation and T_2-relaxation affect the amount of measurable signal in an NMR-experiment (Figure 3.1). Since the transverse component of the net magnetization is detected in an NMR-experiment, the T_2-relaxation decreases the observable signal, in such a way that a faster relaxation decreases the observable signal if the measurement setup is not altered. The effect of the T_1-relaxation on the observable signal is indirect as it does not affect the transverse magnetization. However, since in a usual experiment, the net magnetization does not have time to return to equilibrium before a new excitation pulse, the faster T_1-relaxation leads to an increase in the observable signal.

The relaxation times are generally longer in liquids and thus in soft tissues, making MRI the tool of choice for imaging these tissues. However, in the musculoskeletal system, many tissues are more solid-like, leading to very short T_2-relaxation times, which necessitates the use of specialized MRI methods.

3.3 MAGNETIC SUSCEPTIBILITY

Magnetic susceptibility χ is an inherent property of a material that defines how the material affects the external magnetic field. The effect of the magnetic susceptibility on the external field $\vec{B}_0$ is defined by

$$\vec{B}_{tot} = (1 - \chi)\vec{B}_0, \tag{3.3}$$

where $\vec{B}_{tot}$ is the resulting magnetic field.

The materials can be categorised (roughly) into dia-, para- and ferromagnetic materials based on their magnetic susceptibilities. Diamagnetic materials have $\chi < 0$ and thus they oppose external magnetic fields. Paramagnetic materials have $\chi > 0$ and they reinforce the external field. Ferromagnetic materials have $\chi >> 0$, meaning that they greatly reinforce the magnetic field and become magnetic in the external field (Figure 3.2). Ferromagnetic materials may also retain magnetization on their own after they are removed from the magnetic field.
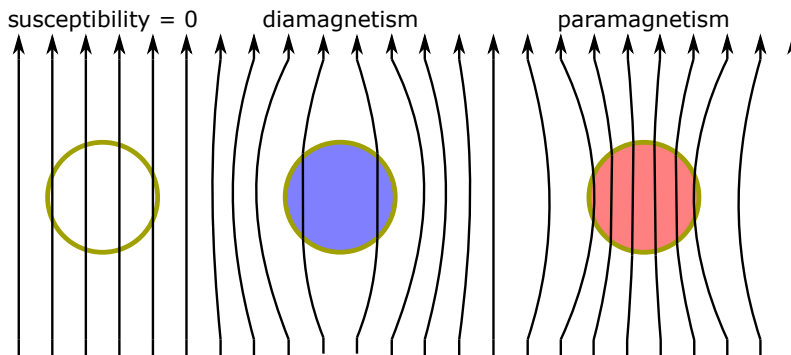
Figure 3.2: The effect of the magnetic susceptibility of a material on the main magnetic field. Diamagnetic materials weaken the external field (field lines are further from each other) and paramagnetic materials strengthen the external field.

Water and most tissues are slightly diamagnetic, but the exact susceptibilities of different tissues are variable, which may either complicate MRI or offer additional benefits, if the susceptibility can be measured.

The varying susceptibilities inside the imaging target will also affect the relaxation properties of the material, namely if the effects of an inhomogenous magnetic field are not compensated for in the imaging sequence, the transverse relaxation may appear faster. This relaxation is termed as T_2^*-relaxation and it includes the ordinary T_2-relaxation and also T_2' components caused by an inhomogenous static field.

3.4 MRI MEASUREMENT

As mentioned earlier, the net magnetization vector needs to be disturbed from the thermal equilibrium to create a measurable NMR-signal. However, simply creating a signal from the target tissue may not be very informative and therefore for imaging purposes, there needs to be a localization of the NMR-signal. This is done by making the main magnetic field spatially variable, which leads to a spatially varying Larmor frequency of the spins. Spatially varying Larmor frequency in turn allows generating a signal from a specific region only, allowing signal localization. The variations in the main magnetic field are called gradient fields. In common MRI, gradient fields are linear and orthogonal. The gradient fields are induced using gradient coils.

The order, type, amplitude and timing of the radiofrequency pulses and field gradients applied during MR imaging are called the pulse sequence. Traditionally pulse sequence consists of an excitation RF-pulse accompanied with a slice (or volume) selection gradient. This is followed by phase encoding gradients and finally by signal acquisition during the frequency encoding gradient (Figure 3.3).

The signal in MRI is acquired as a k-space of an actual MR image in such a way, that the integral of the gradients over time corresponds to the location of the measured signal in the k-space. Thus, if orthogonal gradients are used, one can eventually transform the acquired k-space into a meaningful image by using a discrete Fourier transform.

Most often, we would be interested only in the magnitude image, which displays how much signal we have acquired from a certain location. However, the MR image is actually complex-valued and hence, it contains more information than the plain anatomical (magnitude) image: also the phase angle data of the complex image can be utilized in MRI.

In order to acquire an MR image, the RF-excitation and signal acquisition processes need to be repeated to acquire enough data to allow image formation. In a typical MRI experiment, the time between repetition of the RF-excitation (TR, repetition time) is kept constant during the imaging sequence. The other important timing parameter is the time between the RF-excitation pulse and the signal acquisition (since the signal undergoes relaxation during this period). This parameter is called the echo time (TE). In addition to timing parameters, the angle by how much the RF-pulse tilts the magnetization vector (termed flip angle, α), affects the properties of the MR-image.

3.4.1 3-D Gradient echo sequence

3-D multiecho gradient echo sequence (MGRE) follows the traditional (cartesian) MR-imaging pathway described above. The main differences to the pathway described in previous subsection are that the sequence is 3-D, which necessitates two phase encoding steps into different directions. Moreover, multiple echoes are acquired (Figure 3.3). This leads to an acquisition of multiple 3-D images which have different weightings due to T_2^*-relaxation. The signal magnitude S for an individual echo in the MGRE sequence is of the form

$$S = S_0 \frac{\sin(\alpha) \cdot (1 - e^{-TR/T_1})}{1 - \cos(\alpha)e^{-TR/T_1}} e^{-TE/T_2^*}, \tag{3.4}$$

where S_0 is the spin density of the imaged object. Since TR and α are kept constant during the sequence, it follows that in the MGRE sequence, the first parts of Equation 3.4 are constant and thus individual images from the sequence are weighted by the term e^{-TE/T_2^*}. Thus, from this set of different images, one can calculate T_2^*-relaxation time maps by performing the following voxel-wise minimization

$$T_2^* * = \underset{S_0, T_2^*}{\mathrm{argmin}} \| \sum_{k=1}^{M} S(TE_k) - S_0 e^{-TE_k/T_2^*} \|^2 \tag{3.5}$$

where $S(TE)$ is the magnitude of the signal at each echo time, S_0 is the estimated signal at $TE = 0$ and M is the number of different echo times.

The T_2^*-relaxation time can be calculated from the usual magnitude images; however, one other quantitative parameter (quantitative susceptibility mapping) available from the 3-D MGRE sequence is calculated using the phase data and it will be discussed in more detail in the next section of the thesis.
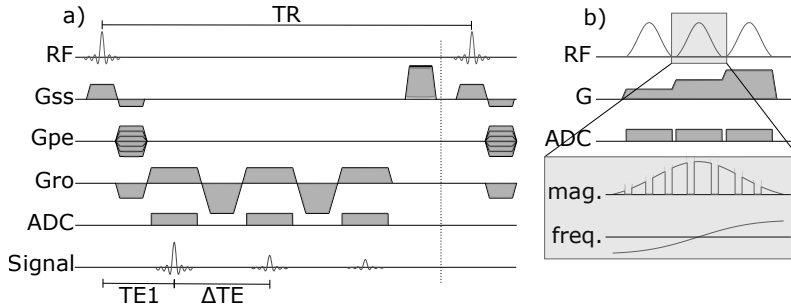
Figure 3.3: a) Pulse sequence diagram for basic multiecho gradient echo sequence with three echoes. The sequence begins with a slice selective RF-pulse having the flip angle α, then gradients along phase encoding directions are applied (G_{ss} and G_{pe}). The signal is acquired while the gradient along the readout direction (G_{ro}) is applied. In this example, a monopolar readout is applied, *i.e.* signal is acquired during positive readouts only. The sequence is repeated until the desired number of different phase encoding steps have been performed. TR is the repetition time, TE1 is time from excitation pulse to first echo and ΔTE is the space between the acquired echoes. b) Pulse sequence diagram for the SWIFT-sequence, The acquisition is performed during the gaps in the frequency swept RF-pulse. Here, hyperbolic secant RF-pulses are displayed as they are used in this thesis. Chirp pulses utilizing linear frequency sweep could also be applied in SWIFT.

3.4.2 Sweep Imaging With Fourier Transform (SWIFT)

In the musculoskeletal system, many tissues have fast or extremely fast T_2^*-relaxations, which necessitates the use of more specialized imaging sequences if these tissues are to be imaged. As the T_2^*-relaxation happens during the TE (and already during the RF-excitation), the obvious answer is to use sequences that are capable of acquiring data very rapidly after the excitation RF-pulse.

These sequences are generally called ultra-short echo time (UTE) sequences, which actually have two main branches. The first branch, referred to here as trueUTE sequences, consists of sequences where the readout gradient is ramped up *after* the

excitation pulse, yielding an extremely short but finite and understandable TE (in the sense, that it can be deliberately manipulated and is not just a delay as required by the transmit and receive (TX) -switching) [41, 42]. The True-UTE-sequences can also be applied in 2-D, a feature that is not possible with the other main branch of UTE-sequences, called zero-echo time (ZTE) sequences [42, 43].

ZTE-sequences differ from the true-UTE in a fundamental way, since in ZTE, the readout gradient is applied before and/or during the RF-pulse [15, 42, 44]. Thus, the only delay in ZTE-sequences consists of the TX-switching, yielding TE that is essentially zero. Due to this difference, ZTE sequences are "limited" to pure 3-D imaging as the RF-pulse cannot be slice selective. Furthermore, the actual TE cannot be easily modified in the ZTE-sequences. However, they are able to detect the signal from even the most rapidly relaxing tissues, such as tooth enamel [45, 46].

One example of ZTE-sequences is the SWeep Imaging with Fourier Transform (SWIFT) sequence [15], in which the frequency swept RF-pulse is used for excitation. Furthermore, the RF-pulse is gapped and the signal is acquired during the gaps of the RF-pulse (Figure 3.3). Due to this acquisition process, the acquired signal has contamination from the RF-pulse and has to be pre-processed to remove the contamination. This is done using a cross-correlation method [47], where the measured signal is deconvolved with the RF-pulse to acquire the correct frequency spectrum of the spin system. After the processing, the real part of the system frequency spectrum corresponds to the spin density profile of the system [15]. The signal intensity of the SWIFT-sequence follows a rather similar equation with the GRE 3.4, the difference being that because SWIFT has almost a zero echo time, the part containing T_2^*-relaxation is insignificant and the signal equation has the form [15]

$$S = S_0 \frac{\sin(\alpha) \cdot (1 - e^{-TR/T_1})}{1 - \cos(\alpha)e^{-TR/T_1}}. \tag{3.6}$$

It can be seen that the T_1-relaxation can be mapped from the SWIFT data, for example by repeating the measurement with different flip angles and solving the following minimization

$$T_1* = \underset{S_0, T_1}{\mathrm{argmin}} \| \sum_{j=1}^{N} S(\alpha_j) - S_0 \frac{\sin(\alpha_j) \cdot (1 - e^{-TR/T_1})}{1 - \cos(\alpha_j)e^{-TR/T_1}} \|^2, \tag{3.7}$$

where $S(\alpha)$ is the measured signal magnitude at flip angle α and N is the number of different flip angles [48, 49].

3.5   QUANTITATIVE SUSCEPTIBILITY MAPPING

In Quantitative susceptibility mapping (QSM), the aim is to map susceptibility distribution inside some region of interest (ROI) based on the MRI-phase data (instead of the much more commonly used magnitude data) [14].

The phase measurement is usually performed using common gradient echo sequences, since they are commonly available on any MRI scanner and do not cancel out the phase modulation induced by susceptibility differences in contrast to spin echo. 3-D data has to be measured as the relationship between the phase and susceptibility is defined only in 3-D [50, 51]. The relationship between the measurable phase and the susceptibility is derived in the following manner.

The relationship between magnetic susceptibility $\chi(\vec{r})$ and the relative difference field (RDF) at location $\vec{r}$ can be formulated as

$$(d * \chi)(\vec{r}) = \frac{B(\vec{r}) - B_0}{B_0}, \tag{3.8}$$

where B_0 is the strength of the applied homogeneous and static external magnetic field, $B(\vec{r})$ is the z-component of the magnetic field at point $\vec{r}$, $*$ is the convolution operator and $d(\vec{r})$ is the z-component of the spatial unit dipole. Furthermore, the above equation assumes that $|\chi| << 1$, $i.e.$ susceptibility changes are very small. $d(\vec{r})$ can be presented as

$$d(\vec{r}) = \frac{3 \cdot \cos^2 \theta - 1}{4\pi \cdot |\vec{r}|^3}, \tag{3.9}$$

where θ is the angle between $\vec{B}_0$ and $\vec{r}$. The value of $d(0) = 0$ due to Lorentz-sphere correction [14]. The right hand side of Equation 3.8, RDF, can be related to the image phase $\phi(\vec{r}; TE)$ of gradient echo type MRI by taking into account the gyromagnetic ratio γ and echo time (TE) of the measurement and assuming no phase aliasing. The relation can be presented as follows:

$$\frac{B(\vec{r}) - B_0}{B_0} = -\frac{f_r}{B_0 \cdot \gamma} = -\frac{\phi(\vec{r}; TE)}{B_0 \cdot \gamma \cdot TE}, \tag{3.10}$$

where, f_r is loosely speaking the rate at which the phase evolves during TE. Finally, by combining equations 3.8 and 3.10 we obtain the relationship between the image phase and the susceptibility

$$-(B_0 \cdot \gamma \cdot TE)(d * \chi)(\vec{r}) = \phi(\vec{r}; TE), \tag{3.11}$$

where TE is the echo time, B_0 is the field strength and $\phi(\vec{r}; TE)$ is the image phase for each voxel at TE. The aim of quantitative susceptibility mapping is to estimate χ from the measured complex data based on Equation 3.11.

The conversion of the phase data to the susceptibility map, however, involves multiple steps (Figure 3.4), detailed in the following subsections. In the following steps of the thesis, the $\vec{r}$ is omitted from the equations for clarity.

3.5.1 Estimation of phase evolution from multiecho dataset

In Equation 3.10, it is assumed that the phase of the MR-image depends only on TE and the phase evolution rate f_r, $i.e.$ $\phi = f_r \cdot TE$. However, it has been observed that the image phase $\phi(TE)$ has a nonzero component at $TE = 0$ that is not related to the susceptibility. The image phase ($\phi(TE)$) can be presented as a sum of the phase evolution (f_r) and the initial phase at $TE = 0$ (ϕ_0). The initial phase, however, is not related to the susceptibility distribution of the target.

$$\phi(TE) = f_r \cdot TE + \phi_0. \tag{3.12}$$

Thus, using the image phase $\phi(TE)$ of single echo imaging in Equation 3.11 does not yield accurate results unless ϕ_0 is negligible. Thus, multiple echoes are typically used to estimate both f_r and ϕ_0 in order to improve the reconstruction of the susceptibility distribution. One method for estimating the phase evolution is the "complex fitting" that is presented in the MEDI-toolbox [52]. The method is based on the following minimization problem
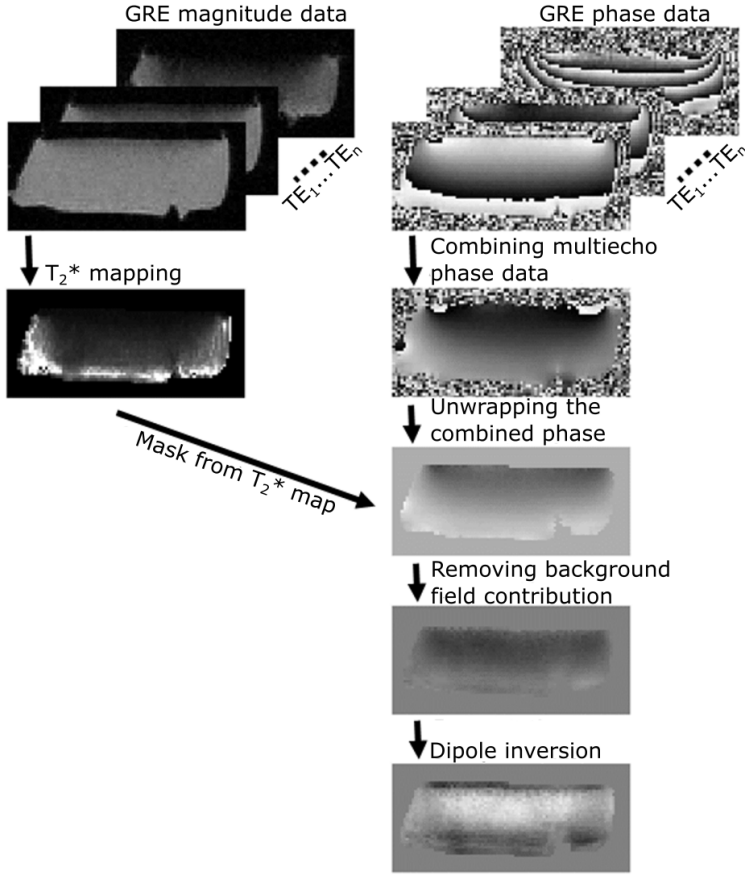
Figure 3.4: The steps in the QSM post processing pipeline as used in this thesis. First, multiecho data was combined to estimate the phase evolution during ΔTE, then the phase was unwrapped and the mask from the T_2^* map was applied. The mask was constructed by allowing only reliable T_2^* relaxation times for the included voxels. After that background field removal and dipole inversion were performed

$$\phi_r*, \phi_0* = \underset{\phi_r, \phi_0}{\operatorname{argmin}} \sum_j \|S_j - A_j \cdot e^{i(f_r \cdot TE_j + \phi_0)}\|, \tag{3.13}$$

where S_j is the measured, complex MRI signal and A_j is the magnitude of the measured signal at the jth TE. There are also many other possibilities to estimate phase evolution [50, 53].

3.5.2 Removal of phase wraps

The second challenge in QSM post-processing arises from the definition of the phase of the complex numbers. The phase of complex numbers is limited between $-\pi$ and π by definition and as a consequence, the phase data of MRI images is wrapped every time, when the phase evolution exceeds the limits (i.e. when the phase evolves

over π it is wrapped back to a value close to -π and vice versa). However, the limitation is obsolete regarding how susceptibility affects the phase evolution of the NMR signal, since susceptibility is not limited in a similar manner. The removal of the wraps might seem to be a trivial process in the first place, but selecting the zero point for unwrapping is non-trivial and thus advanced algorithms for unwrapping the data have been designed [54–56]. The unwrapped phase ϕ is to be solved from the equation

$$\phi = \phi_w + 2\pi n, \tag{3.14}$$

where ϕ_w is wrapped phase and n is positive integer. Thus, estimating the unwrapped phase requires estimating n for every single voxel. One way to estimate n is Laplacian unwrapping [54], which is based on the realization that [57]

$$P = \exp(i\phi_w) = \exp(i(\phi - 2\pi n)) = \exp(i\phi) \tag{3.15}$$

and noting that

$$\mathrm{Im}(1/P\nabla^2 P) = \nabla^2 \phi, \tag{3.16}$$

where ∇^2 is the Laplacian operator and Im denotes the imaginary part of the complex number. Then the Laplacian of the unwrapped phase, $\nabla^2 \phi$ can be solved from the wrapped phase:

$$\nabla^2 \phi = \cos(\phi_w)\nabla^2 \sin(\phi_w) - \sin(\phi_w)\nabla^2 \cos(\phi_w). \tag{3.17}$$

The true phase $\phi(\vec{r})$ can then be solved from Equation 3.17 utilizing Fourier techniques for Laplacian operators, allowing fast solution even for large data sets [54]. The solution is unique by imposing boundary condition that the gradient of n vanishes at the boundary of the ROI and restricting the n to be an integer [54]. Other possibilities to solve phase wraps include *e.g.* homodyne filtering and region-growing algorithms [55,56].

3.5.3 Removal of background field contributions

Since phase and susceptibility are related by convolution, which is a non-local operation, strong susceptibility sources outside the ROI also affect the phase data inside the ROI, causing errors in the estimation of susceptibility maps [58]. The relationship between the measurable phase and relative field change was presented in Equation 3.10. In the following, we simplify the left -hand term in Equation 3.10 as

$$\frac{B - B_0}{B_0} = \Delta f, \tag{3.18}$$

which is the relative field change induced by the susceptibility distribution of interest. However, as Δf and χ are related by convolution, also susceptibility differences that lay outside of the ROI can evoke field changes inside the ROI, *i.e.* the field is a combination

$$\Delta f = \Delta f_{ext} + \Delta f_{loc}, \tag{3.19}$$

where the background field contributions Δf_{ext} can be separated from local field inhomogeneities Δf_{loc} by acknowledging that the external field cannot have sources inside ROI and thus it has to satisfy the Laplace's equation inside the ROI [58]

$$\nabla^2(\Delta f_{ext}) = 0. \tag{3.20}$$

However in discrete MRI imaging, we do not have infinitely thin boundaries between the local and external fields. Thus, removal of background field contributions cannot be directly performed using the Laplace-approach without making assumptions about the phase data or susceptibility at the ROI boundary [58]. Due to this, the estimated susceptibility is often unreliable at the boundary. There are multiple methods to perform the background field removal step; one of these is Projection onto dipole fields (PDF) [59], which is based on estimating background fields via finding a representative susceptibility outside the ROI and assuming constant susceptibility inside the ROI. This is done by solving the following minimization problem inside the ROI

$$\chi_B* = \underset{\hat{\chi}_B}{\text{argmin}} \|w(\Delta f - d * \chi_B)\|, \tag{3.21}$$

where χ_B is the representative susceptibility distribution outside the ROI and w is weighting by noise level estimated from the MGRE magnitude images at different TE's. After solving the minimization, the estimated external field Δf_{ext} can be calculated from χ_B. Ultimately, the local field can be calculated by subtracting the estimated background field from the total field. Other methods for background field removal include, for example, Sophisticated Harmonic Artifact Reduction for Phase (SHARP) [60] and Laplacian Boundary Value (LBV) [61] -methods.

3.5.4 Estimation of susceptibility distribution by dipole inversion

The final step of the QSM post-processing is the estimation of the susceptibility distribution based on the local field map obtained in the previous steps. This problem, however, is mathematically ill-conditioned as the dipole term d in Equation 3.11 has non-trivial zerospace, making the direct inversion of the equation impossible. The relationship between the local field map and susceptibility is presented in the image space as follows

$$\Delta f_{loc} = d * \chi, \tag{3.22}$$

which can be presented also in Fourier-space

$$\mathcal{F}\{\Delta f_{loc}\} = D \cdot \mathcal{F}\{\chi\}, \tag{3.23}$$

where D is the dipole kernel d in Fourier space and $\mathcal{F}\{\}$ denotes discrete Fourier transformation in 3-D. D can be presented as

$$D = \frac{1}{3} - \frac{k_z}{|k|}, \tag{3.24}$$

where k_z is the z-component of the k-space vector parallel to the main magnetic field and $|k|$ is the magnitude of the k-space vector. Formally, χ is easy to solve from Equation 3.23:

$$\chi = \mathcal{F}^{-1}\{D^{-1} \cdot \mathcal{F}\{\Delta f_{loc}\}\}, \tag{3.25}$$

where $\mathcal{F}^{-1}\{\}$ is the inverse discrete Fourier transform. However, it is evident from Equation 3.24 that D has a non-trivial zero space when $\frac{k_z}{|k|} = \frac{1}{3}$ and thus it cannot be inverted as D^{-1}. Thus various approaches exist to solve χ from Equation 3.23 via regularization, but nearly all of them have to make compromises between the computational efficiency and accuracy of the methods. Moreover, finding suitable strength of regularization may not be an easy task [62].

One fast and robust method for performing the dipole inversion is truncated k-space division (TKD) [63]. In TKD, the dipole kernel D is truncated around the zero cone (i.e. the surface where $\frac{1}{3} - \frac{k_z}{|k|} = 0$) as follows

$$D = \begin{cases} \frac{1}{3} - \frac{k_z}{|k|} & \text{if } \|\frac{1}{3} - \frac{k_z}{|k|}\| > \delta \\ \text{sgn}(\frac{1}{3} - \frac{k_z}{|k|}) \cdot \delta & \text{otherwise.} \end{cases} \tag{3.26}$$

The truncation parameter δ can be chosen arbitrarily, providing a trade-off between the numerical accuracy of the susceptibility values and a less noisy image. This truncation approach allows solving the problem extremely quickly, since only one fast Fourier transform and one inverse fast Fourier transform need to be calculated. However, this method leads to an underestimation of the susceptibility, which needs to be corrected [64]. This correction is done by scaling the susceptibility values with the point spread function of the truncated kernel. The correction for the susceptibility underestimation makes possible the use of large truncation parameters in TKD, which in turn improves the noise-tolerance of the method without underestimating susceptibility [64].

Furthermore, it needs to be addressed, that in the QSM research, there is much ongoing research aiming at optimizing the processing pipeline [58,62]. One focus of this work has been to combine the aforementioned steps in the pipeline and to resolve joint problems. Examples of these are HARPERELLA [65], which combines the unwrapping of the phase and background field removal steps and TFI [66], which combines background field removal and dipole inversion steps. Finally, since in clinical imaging the multicoil imaging techniques are routinely used and furthermore in clinical imaging, the focus has been on magnitude images, all methods that are suitable for combining magnitude images may not be suitable for combining phase data. Thus, suitable methods for coil combination for QSM need to be considered, *e.g.* the popular sum-of-squares technique [67] is not generally suitable [50]. Possible coil combination methods include phase difference and phase image reconstruction methods [50].

4   MRI of articular cartilage

MRI is one of the main tools used in the diagnostics and staging of osteoarthritis and related diseases. In this chapter, I will first review shortly how MRI has been applied in cartilage imaging and then introduce more specifically what has been done with QSM, T_2^*-relaxation time mapping and UTE- and SWIFT-imaging.

4.1   CONVENTIONAL MRI OF ARTICULAR CARTILAGE

In general, MRI is a widely used tool for cartilage imaging in clinics [68]. MRI has good contrast in soft tissues and thus it is well suited for imaging cartilage. In the clinic, MRI is usually applied for anatomical imaging of joints, and from those images, one can evaluate cartilage thickness or cartilage loss as well as detecting ligament injuries and bone cysts [68, 69]. Moreover, semiquantitative scoring systems, such as MRI Osteoarthritis Knee Score (MOAKS) are based on anatomical imaging [70]. However, anatomical imaging is mostly useful in resolving how badly tissues have become damaged during the progression of osteoarthritis and the early changes caused by the disease are often not observable with MRI. This is also likely due to the fact that symptomless joints are rarely imaged and usually as the patient starts to experience symptoms, OA has already progressed [4, 69, 71].

As mentioned earlier, multiple quantitative parameters can be mapped by MRI and a number of these parameters have been used for the evaluation of articular cartilage both preclinically and in clinical studies. The quantitative parameters that have been proposed and applied for cartilage imaging include a measurement of relaxation times, *e.g.* T_1, T_2, and $T_{1\rho}$ relaxation times [72–76], delayed gadolinium enhanced MRI of cartilage (dGEMRIC) [77–79], diffusion weighted and diffusion tensor imaging [80, 81], glycosaminoglycan specific chemical exchange saturation transfer (gagCEST) [10, 82] and sodium imaging [83].

If one considers these methods, it is evident that some are more sensitive towards the proteoglycan content of cartilage while others depend more on the properties of the collagen network. GagCEST, sodium imaging and dGEMRIC correlate especially well with the proteoglycan content. On the other hand, diffusion imaging reflects the properties of the collagen fiber network of cartilage. With respect to the relaxation time measurements, T_2 relaxation is thought to be more dependend on the collagen network and $T_{1\rho}$ on the proteoglycan content. However, especially for $T_{1\rho}$, the results depend heavily on the specific measurement protocol [74, 84]. Native T_1 imaging is less widely used in cartilage imaging and the main application for T_1 relaxation time mapping has been within the dGEMRIC experiment.

Although these quantitative MRI methods can probe articular cartilage rather well, nearly all of them have their drawbacks, warranting new studies utilizing new contrast mechanisms. For example, gagCEST can be time-consuming to image with high resolution, causing patient discomfort and increasing the probability of motion artefacts. Moreover, gagCEST is sensitive only towards the proteoglycan concentration, not disruptions in the collagen network (which can be regarded as an advantage in some situations) [10]; sodium-MRI requires special hardware (sodium

coils and RF-amplifiers) and special sequences that are also time-consuming [83]; dGEMRIC is slightly invasive (contrast agent injection) and requires that there is a sufficient time between the pre- and post-contrast images [77]; diffusion measurements may also require long scan times and they need to be well designed for application in cartilage imaging since for example, the collagen network of cartilage does not restrict diffusion as extensively as myelin sheets. Finally, relaxation times, which depend on the field strength and measurement setup, are mostly sensitive to tissue degeneration rather than specific properties that are changing in cartilage during OA (which might also be beneficial in some cases). Some of these parameters, especially relaxation times, also depend on the orientation of cartilage in the magnetic field [84,85]. This is called the magic angle effect, which is caused by water molecules that are strongly aligned with the collagen fiber orientation, causing their T_2 relaxation time to depend on the orientation of the collagen fibers in the magnetic field [85]. The magic angle effect causes a notable increase in the affected relaxation times, and may lead to misdiagnosis if not properly taken into account. The magic-angle effect is most clearly observed when the collagen fibers are near to an angle of 54.7° with respect to the magnetic field [84,85]. To overcome certain limitations, namely the time consuming imaging and the need of specific hardware or contrast agent injections, the use of QSM is proposed in this thesis and also elsewhere [86–88].

4.2   QUANTITATIVE SUSCEPTIBILITY MAPPING

QSM has been seldom studied in the musculoskeletal system and especially in articular cartilage. Many of the studies of cartilage applying QSM have concentrated on imaging the vasculature in the epiphyseal cartilage or the growth plate and are not the focus of this study [89–91]. To date, there are only a couple of studies probing QSM of mature articular cartilage outside of this thesis [86–88]. The first study investigating this topic showed that anisotropic susceptibility of collagen fibers caused QSM to be also anisotropic in articular cartilage [86]. Furthermore, that study demonstrated that QSM had depth-wise contrast in cartilage and that this contrast seemed to correlate with the collagen fiber orientation at the different layers of articular cartilage. More specifically, the susceptibility in articular cartilage was highest nearby to or at the superficial layer of articular cartilage and decreased towards the deeper layers. A follow-up study went one step further and utilized susceptibility tensor imaging (STI) [92] to show that susceptibility contrast could be used to map the collagen fiber orientation in articular cartilage [87]. However, the use of STI is problematic since it requires imaging of the target at multiple (more than 6) physical orientations of the sample with respect to the main magnetic field, which should also be relatively well distributed in all three dimensions (*i.e.* the target has to be rotated with respect to all axes) [92]. Clinical studies [88] have shown that QSM contrast in articular cartilage in the osteoarthritic knee joint is altered in such a way that OA reduces the depth-wise variation in the susceptibility of cartilage.

   This thesis differs from the previous studies in that here, selective degradative treatments were applied on osteochondral samples to determine if and how the different cartilage constituents affect the QSM contrast in cartilage and in study **II**, samples with degeneration due to post-traumatic osteoarthritis were scanned. Additionally, several reference methods to resolve the degenerative state of the tissue

samples were used. Thus, this study is the first that has attempted to relate QSM with the progression of OA in articular cartilage and the specific compositional changes associated with it.

4.3 T_2^* RELAXATION TIME MAPPING

T_2^* relaxation time has been used to probe similar properties in articular cartilage as the more common T_2 relaxation time; these include probing the collagen network structure and evaluating the water content of cartilage [75, 93, 94]. However, since shorter echo times can be used in T_2^* relaxation time mapping, this approach may better reflect the properties of the fast relaxing spins than T_2 relaxation time mapping. On the other hand, T_2^* relaxation time mapping is more prone to errors caused by an inhomogeneous magnetic field. An additional benefit of T_2^* relaxation time is that it can be readily used within ultra-short echo time sequences, and they have already been demonstrated to provide a robust measurement of T_2^* relaxation time in the deepest cartilage regions [11, 95]. Although T_2^* relaxation time and QSM are similar in the sense that both are affected by the magnetic field inhomogeneities, they also complement each other very well. While the T_2^* relaxation time measurement essentially contains the information from the T_2 relaxation time that is affected by field inhomogeneities, QSM probes directly the cause of these field inhomogeneities (*e.g.* susceptibility changes within the tissue) directly. AAs mentioned, both parameters can be measured in the same sequence at the same time. However, until this work, no studies combining the information from T_2^* relaxation time mapping and QSM had assessed the structural and mechanical properties of articular cartilage.

4.4 ULTRA-SHORT ECHO TIME IMAGING

Ultra-short echo time imaging of articular cartilage and other musculoskeletal tissues has become increasingly popular within the last ten years. The reason behind its popularity lies in the fact that this technique has a unique ability to measure the signal from tissues which have extremely fast T_2^* relaxation, *i.e.* many tissues of the skeletal system. UTE-imaging has been used for both anatomic imaging of joints and osteochondral samples [11, 43, 96] and for quantitative parameter mapping, such as T_2^* and $T_{1\rho}$ relaxation time mapping [17, 49, 95, 97, 98]. UTE-sequences have been especially useful in the quantitative assessment of the deepest regions of articular cartilage, since fast relaxation in that region complicates the imaging using sequences with conventional echo times [11]. Quite specifically, a bright signal feature has been observed at the osteochondral interface when using ultra-short echo time sequences. The signal has been proposed to originate from the calcified cartilage, that has been previously unseen by conventional MRI [96]. Naturally, this observation has attracted attention and the relaxation properties of this signal have been probed using UTE-sequences [17, 99]. Furthermore, it has been shown that this feature is diminished near to bone marrow lesions [100]. However, studies on the exact location of this signal have not been conducted, since previously it has only been localized by matching of thin histology slices with thick MRI slices [96, 99]. Thus, the precise origin and changes in the signal due to OA processes remain to be clarified. While one can speculate that changes take place at the osteochondral junction in OA and measuring these might be even more relevant than assessing the changes in cartilage, it is nonetheless important to understand, which changes can

affect this hyperintense signal. Thus, it is of extreme importance to precisely localize this signal by combining the information from SWIFT-MRI with the information from μCT imaging, which sees the calcified cartilage as bone [101].

5   Aims and hypotheses

Methods for early detection and follow-up of osteoarthritis need to be found if effective disease-modifying drugs or surgical treatments are to be developed or if the progression of OA is to be predicted. MRI offers ways of quantifying numerous parameters describing the properties of articular cartilage, but at present, none of these MRI parameters seem to have a truly excellent ability to predict OA progression or to robustly detect very early degenerative changes.

The hypotheses of the study were that QSM can represent a fast and quantitative 3-D MRI method for the assessment of articular cartilage and that it would be sensitive to the osteoarthritic changes in the extracellular matrix of articular cartilage. For the studies regarding the osteochondral junction, it was hypothesized that the hyperintense signal observed in SWIFT-MRI is located in the deep uncalcified cartilage. Further, it was hypothesized that the hyperintense signal is generated by the fast T1 relaxation at the osteochondral junction and in part by the susceptibility difference between the uncalcified cartilage and the calcified cartilage.

Thus, the aim of this thesis was to evaluate QSM and SWIFT-methods, for imaging and evaluation of articular cartilage. The specific aims of the studies comprising the thesis were:

1. To study how to perform QSM in articular cartilage in a reliable way and to evaluate how susceptibility depends on the condition of the cartilage and what kind of orientation anisotropy it may exhibit.

2. To correlate QSM and T_2^*-relaxation with biomechanical properties, proteoglycan content and collagen network properties of equine cartilage suffering from post-traumatic osteoarthritis.

3. To precisely localise and provide plausible explanations for the hyperintense signal seen at the osteochondral junction with SWIFT-MRI.

6 Materials and Methods

6.1 SAMPLES AND SAMPLE PREPARATION

Different osteochondral samples were utilized in each of the studies. In study **I**, cylindrical plugs obtained from the patellae of three skeletally mature bovines were used. In study **II**, wedge shaped samples from the medial trochlear ridges of equine subjects were utilized. In study **III**, cylindrical plugs from tibial cartilage of a cadaver human donor were investigated.

In study **I**, a total of 9 cylindrical osteochondral samples (diameter = 6mm) were drilled out of the patellae of skeletally mature bovine knee joints, acquired from a local grocery store. After the samples were dissected, they were immersed in phosphate buffered saline (PBS) and stored in a freezer (-20°C). The samples were subjected to different enzymatic/physical treatments to induce variable changes in the composition of cartilage prior to imaging. Three of the samples were left untreated. Two samples were degraded with trypsin to induce a loss of proteoglycan in the osteochondral samples. The trypsin treatment was performed by immersing the samples in 0.5mg/ml trypsin solution (Sigma Aldrich, trypsin from bovine pancreas). The solution was then placed in an incubator (temperature=37°C; CO_2=5%) for nine hours. The degradation was stopped by immersing the samples in PBS containing enzyme inhibitors. Two of the samples were first treated similarly with trypsin, but also additional degradations (heat or enzymatic treatment) to induce also changes in the collagen network were performed; one sample was degraded with collagenase enzyme in an incubator (30 units/ml, Sigma Aldrich Collagenase Type VII from Clostridium histolyticum, treatment time=22h; temperature=37 °C; CO=5%) and the other was degraded thermally in a sealed, PBS-filled test tube in a water bath at 60 °C for 15min. The remaining two samples were decalcified with ethylenediaminetetraacetic acid (EDTA) prior to imaging.

In study **II**, 20 wedge-shaped osteochondral samples from the medial trochlear ridges of equine specimens were utilized (Figure 6.1). Samples were gathered from both stifle joints of 10 animals. Fourteen of these samples were originally from an equine cartilage repair study [102], where lesions were surgically induced in both medial trochleae of the horses and the lesions were repaired with a combination of chondrons and mesenchymal stem cells in different carrier hydrogels. As a result, the horses developed post-traumatic osteoarthritis in the tissue surrounding the lesions [103]. One year after the repair, the animals were sacrificed and wedge-shaped samples which partially covered the lesion area were harvested. Six control samples were prepared from the stifle joints of horses obtained from a slaughterhouse. The control animals had a matching age range with the experimental animals [103]. In this study, the biomechanical testing was conducted on the samples prior to the MRI assessment. Moreover, the samples underwent also optical measurements, the results of which have been reported elsewhere [103,104].

In study **III**, eight cylindrical osteochondral plugs with a diameter of 4 mm were prepared from the tibial cartilage of one human cadaver. Four samples were from the medial and four from the lateral tibia. The samples were stored in a freezer after

the preparation. Furthermore, one plug from tibial cartilage of bovine knee was studied in more detail with more time consuming imaging as the human samples had to be scanned rapidly, since the samples were part of a larger study which had a tight schedule. One sample from the dataset had to be rejected due to extreme motion artifacts during MRI.
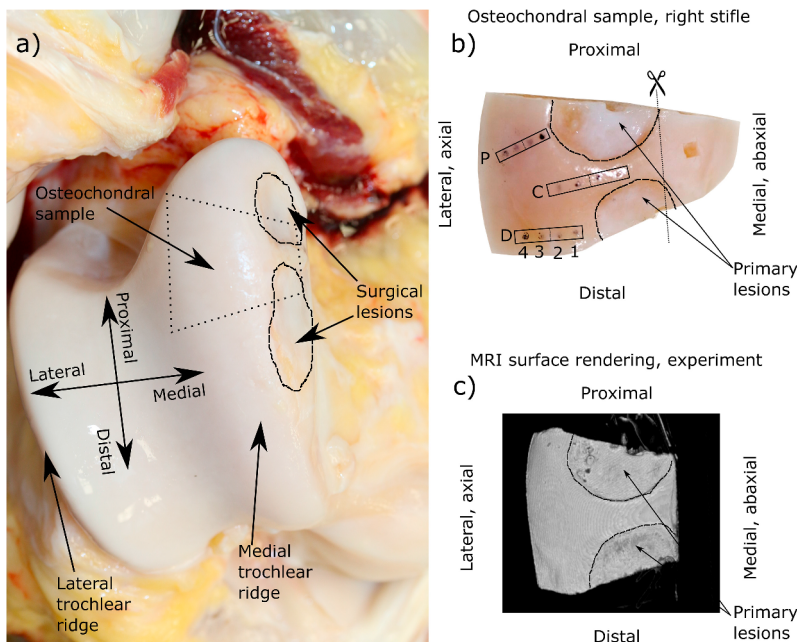
Figure 6.1: Preparation of the osteochondral samples in study **II**. A wedge shaped osteochondral sample was prepared from the area in the vicinity of the surgical lesions. Before MRI, the sample was cut to fit it into the magnet.

6.2 MRI MEASUREMENTS

In all the studies, the MRI was performed using a 9.4T Varian/Agilent scanner (Vnmrj DirectDrive software v. 3.10). In studies **I** and **II**, a 19-mm-diameter and in study **III**, a 10-mm-diameter quadrature RF volume transceiver (Rapid Biomedical GmbH, Rimpar, Germany) were utilized. During the imaging, the samples were immersed in [1]HMRI-signal-free perfluoropolyether. In study **I**, the samples were attached in a custom-built holder that allowed rotation of the samples with respect to the main magnetic field, allowing the examination of the orientation anisotropy of the samples. In studies **II** and **III**, the samples were placed in plastic test tubes.

In studies **I** and **II**, the MRI was performed using a 3-D MGRE sequence to allow mapping of both susceptibility differences and T_2^* relaxation times of the samples. The sequence had the following parameters: TR = 150 ms, α = 23°, TE_1 = 2.00 ms, ΔTE = 3.05 ms, number of echoes = 6, bandwidth = 150 kHz. In study **I**, the image matrix size was 192^3 voxels and the voxel size was $(94\mu m)^3$. In study **II**, the matrix size was 200x256x200 voxels and the voxel size was $(100\mu m)^3$. In study **I**, imaging was repeated in five different orientations (0°, 25°, 45°, 65°, and 90°) of the

sample surface normal with respect to the main magnetic field of the scanner. In study **II**, the sample was oriented in such a way that the angle between the surface normal and main magnetic field was approximately 90° throughout the sample to avoid effects caused by susceptibility anisotropy.

In study **III**, MRI was performed using the SWIFT-sequence with different saturation pulses (and variable flip angles for the bovine specimen). SWIFT data was acquired using a gapped hyperbolic secant pulse and the following imaging parameters: TR =2.6s, bandwidth = 62.5kHz, $\alpha = 6°$, matrix size = 384^3 voxels and voxel size = $(65 \ \mu\text{m})^3$. Different spectral saturations were obtained by applying 20 ms 180° hyperbolic secant pulses with 1 kHz bandwidth at a specified offset frequency (+/- 1400, or 0 Hz) after every sixteenth repetition. One dataset was imaged with a 20 ms delay in place of the saturation pulse to image all the signals from the specimen without saturation, but to maintain equal timing and thus a comparable signal level. The aim of the spectral saturations was to allow reconstructing images of short- and long-T_2^* spin pools separately in order to allow careful examination of the short-T_2^* signal feature in the vicinity of the osteochondral junction. Differently saturated images were also used to create images where the signals from all the spin pools were reconstructed in-focus, meaning that also the signal from fat was reconstructed without radial blurring. These hybrid SWIFT images are termed Short-T_2^* and all-in-focus images throughout this thesis respectively (see section 6.4 and Figure 6.3). The bovine specimen was also imaged using different flip angles to allow T_1-relaxation time mapping. As the SWIFT data is acquired radially, the images could not be reconstructed using standard fast Fourier transform. Thus, the images were reconstructed from the acquired 262144 radial spokes per imaged volume by regridding the spoke data on a cartesian grid.

After MR imaging, all the samples were first fixed in 10% neutral buffered formalin for 48 hours and then decalcified in EDTA. After decalcification the samples were processed into histological sections.

6.3   REFERENCE MEASUREMENTS

All individual studies had slightly different sets of reference measurements, consisting of light microscopy of stained histological sections from the samples, polarized light microscopy, optical density measurements, biomechanical testing and μCT imaging. The histological stainings utilized in the study were safranin-O staining, hematoxylin and eosin stain (H&E) and Masson's trichrome staining. The safranin-O and H&E stainings were used in study **I** in a semi-quantitative light microscopic assessment, as the intensity of safranin-O stain reveals the proteoglycan content of the cartilage and H&E stain allows straightforward distinction between articular cartilage, calcified cartilage and subchondral bone. The pixel size for the histological images in study **I** was $(3.5 \mu\text{m})^2$.

In study **II**, digital densitometry of the safranin-O stained slices was performed to measure their optical density, which is related to the proteoglycan content of the articular cartilage. Digital densitometry was performed using a light microscope equipped with a monochromatic light source and a CCD-camera with the following settings: objective 1x, zoom 2x, binning 1 and calibration with neutral density filters of 0–3.0 optical density. Then, the optical density of each sample was calculated based on the calibration set.

Part of the histological sections were left unstained and instead they were treated

with hyaluronase to remove proteoglycans from the sections. These sections were then imaged utilizing polarized light microscopy (PLM). PLM was used as a reference method in studies **I** and **II** to reveal the collagen fiber angle and collagen network anisotropy in the histological sections of the samples. In the PLM measurements an Abrio PLM imaging system (CRi Inc., Woburn, MA, USA) which was mounted on a light microscope (Nikon Diaphot TMD, Nikon Inc., Shinagawa, Tokyo, Japan) was used with the pixel size of $(3.5\mu m)^2$. As the system did not allow direct imaging of the collagen network anisotropy (A_{PLM}), it was calculated from the fiber angle as follows

$$A_{PLM} = \frac{1}{1+\epsilon},$$ (6.1)

where ϵ is the image entropy of the fiber angle image in a 5x5 pixel neighbourhood of each pixel.

In study **III**, Masson's trichrome was used instead of the H&E staining in order to distinguish between the different regions of the osteochondral sample. The Masson's trichrome -stained slices were imaged with a digital pathology slide scanner (40x magnification and $(0.25\mu m)^2$ pixel size; Aperio AT_2, Leica Biosystems, Wetzlar, Germany).

Another reference method used in study **II** was biomechanical testing, based on which the equilibrium and dynamic moduli of articular cartilage could be calculated. The biomechanical testing was performed using a system that had a 250g load cell (accuracy $\pm$ 0.25%, Model 31, Honeywell Sensotec Sensors, Columbus, OH, USA) and an actuator (displacement resolution 0.1μm, PM500-1 A, Newport, Irvine, CA, USA). In the study, biomechanical testing was performed at 12 locations of each individual osteochondral sample [103]. Measurements at adjacent locations in quick succession did not affect the results of the testing as the utilized intender was small when compared to the distance between the measurement locations [105].

In study **III**, high-resolution μCT imaging was utilized as a key reference to allow precise localization of the hyperintense SWIFT signal. μCT imaging was performed using a Skyscan 1272 device (Bruker microCT, Kontich Belgium) by using an x-ray tube voltage of 50kV and 200μA current, and 0.5mm aluminum filtering. 1200 projections with 2200ms exposure time and three times frame averaging were collected. Projections were reconstructed to images with isotropic $(2.75\mu m)^3$ voxel size with NRecon-software (v.1.6.10.4, Bruker microCT) utilizing beam hardening and ring artifact corrections.

6.4   DATA ANALYSIS

Prior to data-analysis, parameter maps were estimated in studies I and II. In both studies T_2^* relaxation time maps were calculated by solving the minimization problem in Equation 3.5 using the in-house devised Matlab (Mathworks, Inc) algorithm, which was based on linearizing the problem and limiting the maximum value of T_2^* relaxation time to 150 ms. The limit was applied since the utilized echo times were somewhat low, which led to an occasional over-estimation of long T_2^* relaxation times.

In studies **I** and **II**, the QSM post processing pipeline started by using the "complex fitting" -method from the MEDI-toolbox [106] to estimate the phase evolution from multiecho data [52] and the Laplacian method was applied for phase unwrapping [54]. In study **I**, the PDF method was used for the background field

removal [59] and dipole inversion was calculated using the TKD method with correction for susceptibility underestimation [63, 64]. Even though the results achieved by utilizing this pipeline were generally good, the cartilage in the equine samples was so thin in study **II**, that it was crucial to avoid erosion of the boundary voxels in the background field removal step. Thus, in study **II**, the TFI algorithm, which solves background field removal and dipole inversion simultaneously, was utilized [66].

In each study, the basis for the data-analysis were depth-wise parameter value profiles or intensity profiles calculated from the MRI-data and reference images (PLM, optical density and μCT). In studies **I** and **III**, the profiles were calculated as averages from cylindrical ROI with a radius of 1 mm, at the midpoint of the cylindrical plugs. The PLM profiles in study **I** were calculated as an average of three histological slices at the midpoint of the sample. In study **I**, the anisotropy profiles were calculated as Michelson contrast between the profiles collected from the data that was imaged at different orientations of the sample. Michelson contrast A at location (depth) r is defined as [107]

$$A(r) = \frac{P_{max}(r) - P_{min}(r)}{P_{max}(r) + P_{min}(r)},$$
(6.2)

where $P_{max}(r)$ and $P_{min}(r)$ are maximum and minimum values of the parameter P at depth r through all orientations. Since in QSM, parameter values are distributed around 0, Equation 6.2 was modified to use global maximum and minimum values in the denominator instead of the local values to avoid division by zero. In study **II**, similar profiles were calculated, but instead of using only one profile per sample, the profiles were collected around each biomechanical testing point of the samples. The profiles were collected by applying Matlab algorithms that were based on selecting a point around which a circle with an appropriate radius was defined. Then the MRI and/or μCT values were sampled along the normal of this circle throughout the cartilage depth. The profiles from the images acquired with different modalities were interpolated into matching lengths in each study to allow more precise analysis.

In study **I**, the profiles from different modalities and differently treated samples were qualitatively compared with each other, to determine the differences or similarities between them. In study **II**, a more quantitative analysis was made to investigate whether either QSM or T_2^*-mapping could be linked to the progression of post-traumatic osteoarthritis or correlated with the reference properties of articular cartilage. The statistical methods applied in study **II** are more described in more detail in the next section. In study **III**, the intensity profiles from co-registered hybrid SWIFT images and μCT images (Figure 6.3) were calculated and compared to find the exact location of the hyperintense SWIFT signal with respect to the bony structures visible in the μCT images.

In study **III**, it was of extreme importance that the MRI and μCT images were registered as precisely as possible. This was achieved by co-registering the MR- and μCT images using the affine transform in elastix-software [108] and applying maximizing of the mutual information of the images as a cost function. In the co-registration, all-in-focus MR images with inverted contrast and background masking were created to maximize the similarity of the contrast between the MR- and μCT-images (Figure 6.2) to aid in the automatic co-registration. The transform parameters from the co-registration were then utilized to co-register the rest of the MR-images

acquired from the same sample in the same geometry. In the end, the success of the co-registration was confirmed visually.
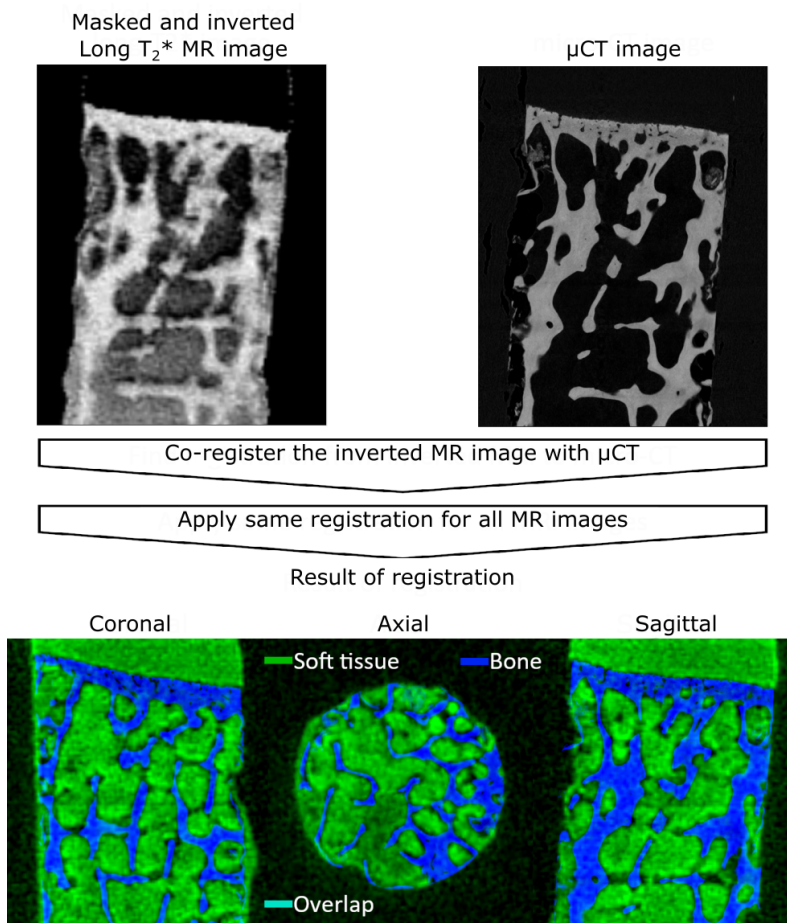
Figure 6.2: The co-registration process in study **III**. First, inverted contrast MRI image having similar contrast with μCT was created. Then co-registration between inverted contrast MRI and μCt was performed. The same registration parameters were then applied for all MR-images. In the images of the bottom row, the soft tissue (green color) depicts MRI intensity and bone (blue color) depicts μCT intensity.

6.5 STATISTICAL METHODS

In study **II**, the MRI-parameter profiles were used to predict the reference variables (i.e., equilibrium and dynamic moduli, proteoglycan content, collagen fiber angle and collagen anisotropy) using partial least squares regression (PLSR) [109]. Prior to the PLSR-analysis, the depth-wise profiles were normalized using standard normal variate [110] and to avoid overfitting of the models, the analysis was performed using 10-fold cross-validation. The PLSR-predictions of the reference parameter values were compared with the measured reference parameter values with Spearman's

rank correlation analysis [111]. Direct correlations were also calculated between the means of full and superficial (25% depth) T_2^* relaxation time profiles and the reference parameter values as a way of comparing the results of PLSR-analysis with the more conventional analysis. For QSM, Spearman's correlation coefficient was calculated between the range of the susceptibility values and the reference properties. Range was utilized for QSM instead of the mean, since the mean value of QSM tends to remain near to zero, especially in full thickness ROI's.

The statistical significance of the differences in the tissue properties between the experimental and control groups was tested with Mann–Whitney U test [112] in SPSS (Version 25, SPSS Inc., IBM Company, Armonk, NY, USA). For the profile data, this analysis was performed at each point of the depth-wise profiles. Statistical significance of Spearman correlations was tested using exact permutation distributions (see *e.g.* [113]) in Matlab. In both tests $P < 0.05$ was considered as the limit for statistical significance. Non-parametric tests were applied since the reference parameter data was non-normally distributed as per the Shapiro–Wilk test [114] ($P < 0.0001$).
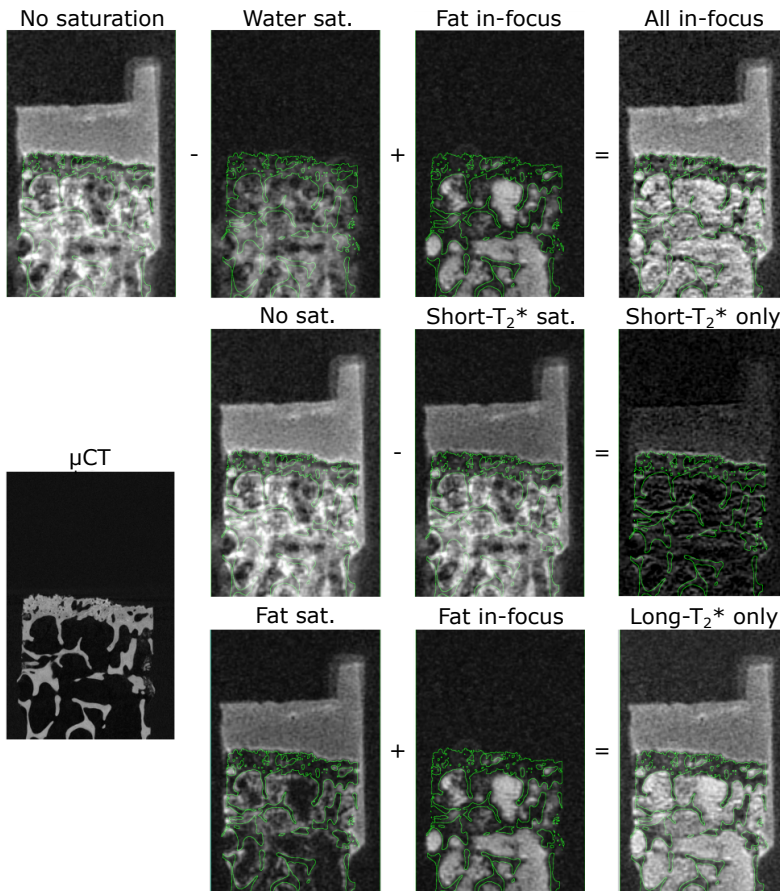
Figure 6.3: The hybrid SWIFT images created for the study III. In addition, the μCT image is displayed and the outline of the bony structures visible within it is displayed with green color overlays in the MR-images.

6.6 SUSCEPTIBILITY SIMULATIONS

In study **I**, simulations on the anisotropy of susceptibility were performed, since the observed QSM anisotropy seemed unexpected compared to the T_2^*-relaxation time anisotropy. In the simulations, cylindrical layered susceptibility distribution, mimicking the distribution observed for cartilage at $0°$ orientation with respect to the main magnetic field was created (Figure 6.4). Then, the magnetic field perturbation generated by this susceptibility distribution was calculated using Equation 3.23 at different orientations between the susceptibility distribution and the main magnetic field, and gaussian noise was added to the realizations. Subsequently, QSM post-processing was performed on the simulated field maps using the PDF and TKD methods.

Initial susceptibility distribution
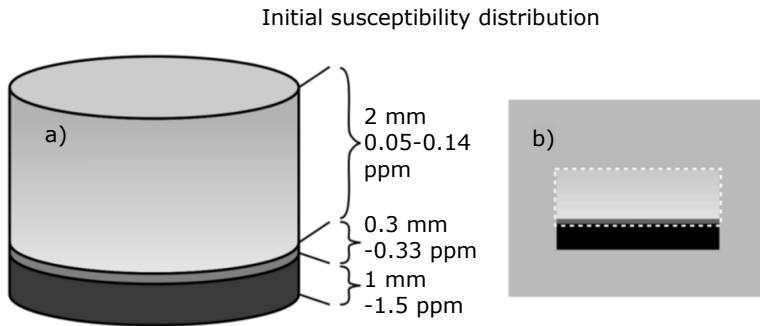
Figure 6.4: The susceptibility distribution generated for the susceptibility simulations. a) The susceptibility distribution in the cylinder and b) a vertical slice of the distribution. The white dashed line marks the ROI utilized in the QSM processing phase of the simulations.

7 Results

7.1 REFERENCE MEASUREMENTS

In study **I**, the aim was to induce different kinds of degeneration in the specimens to evaluate how this would be evident in the QSM data. The safranin-O stained histological slices revealed that the trypsin treatment had removed almost all of the proteoglycans from the articular cartilage. Furthermore, the PLM images revealed that trypsin treatment had caused slight damage to the superficial collagen network. Moreover, PLM revealed that collagenase treatment had eroded the superficial collagen fibers and the thermal treatment had evoked disruptions in the collagen fiber network throughout the sample (Figure 7.1).
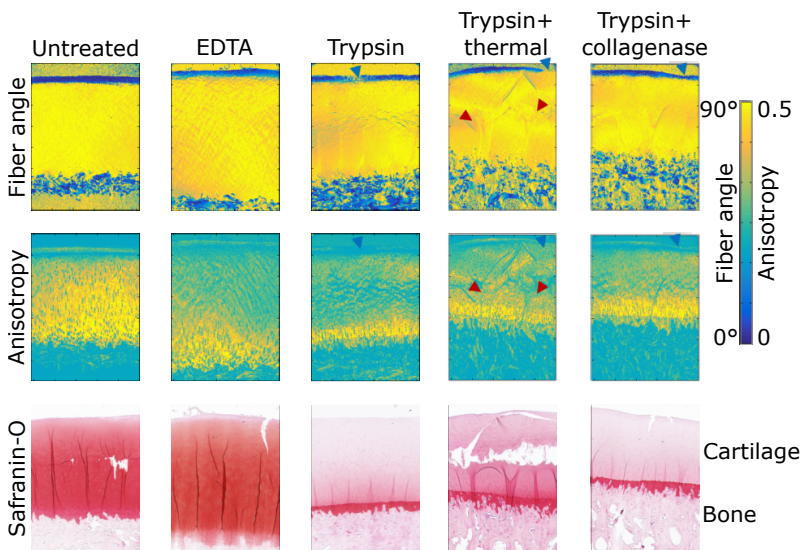
Figure 7.1: Reference measurements from bovine samples after different degradative treatments. It can be seen, that trypsin has removed most of the proteoglycans in the cartilage. The thermal treatment caused a disruption of the collagen network throughout the cartilage thickness.

In study **II**, all reference properties (i.e. equilibrium and dynamic moduli, proteoglycan content, collagen fiber and collagen fiber anisotropy) were altered between the experimental and control samples. The equilibrium and dynamic moduli were significantly higher in the control group in most of the measurement points (see Figure 2 in study **II**). The proteoglycan content was significantly higher in the control group at those locations, which were nearby to the induced lesions in the experimental group (Figure 7.2). The collagen fiber angle in the deep cartilage was also significantly decreased in the experimental group at the measurement points in the vicinity of the lesions (Figure 7.2). The collagen fiber anisotropy, on the other hand,

was only significantly decreased in the experimental group at the points furthest away from the lesions (Figure 7.2). It was also noted that the PLM fiber angle did not display typical behavior, where the superficial layer covers a small percentage of the total depth of the cartilage but instead the collagen displayed a superficial orientation nearly throughout the cartilage at the measurement locations near the surgical lesions (Figure 7.2). Similar behavior was noted at the same anatomical locations in the control samples, which can be explained by the fact that this anatomical location was near to the peripheral region of the stifle joint.
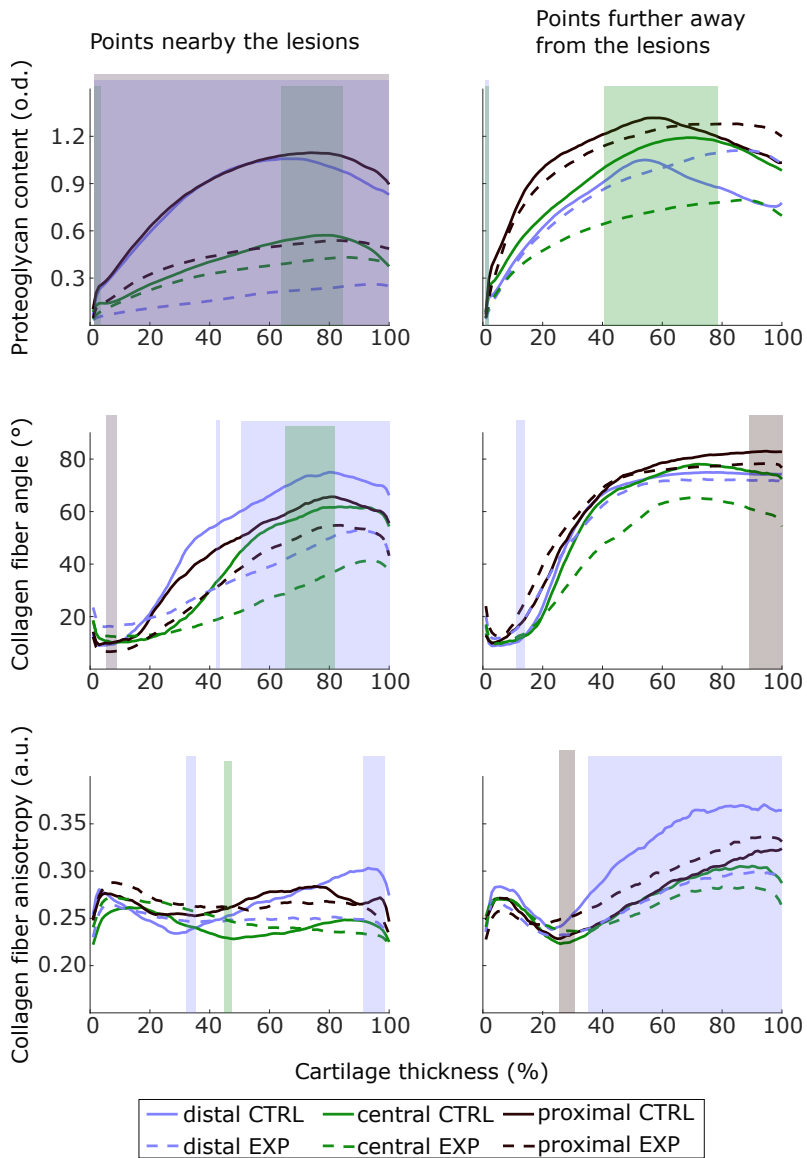
Figure 7.2: Reference properties of the equine samples at different measurement locations. The difference between the experimental and control results is statistically significant at the locations indicated by the shaded areas.

7.2 QUANTITATIVE SUSCEPTIBILITY MAPPING

Probably the most important result regarding QSM of articular cartilage, which was the main topic of this thesis, was that QSM is not very sensitive towards specific degenerative changes in articular cartilage. In study **I**, it was observed that different degradative treatments did not drastically affect the QSM (Figure 7.3). Furthermore, the anisotropy of QSM seemed to be almost unaffected by the treatments. The magnitude of the susceptibility anisotropy was also generally low but was clearly increased as one moves towards the osteochondral junction (Figure 7.4). Generally, the QSM contrast in articular cartilage was such that the susceptibility was near zero at the surface of the cartilage, increased towards the middle of cartilage and then declined sharply towards the osteochondral interface at 0° and 90° orientations (Figure 7.6). At the orientations near the magic angle (55°), the susceptibility remained near zero throughout the cartilage depth (Figure 7.6).
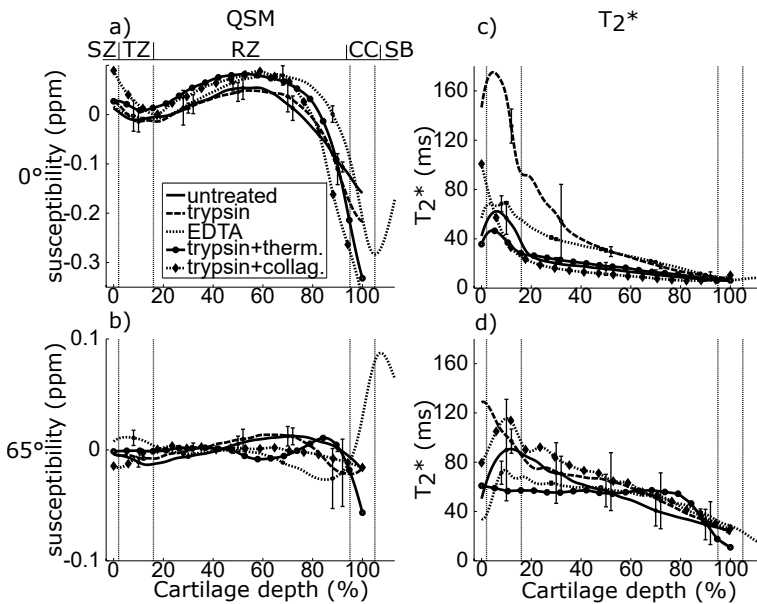
Figure 7.3: The susceptibility and T_2^* relaxation time profiles through cartilage at different imaging orientations following different degradative treatments. The bar above the first graph indicates the cartilage zones: SZ = superficial zone, TZ = transitional zone, RZ = radial zone, CC = calcified cartilage, and SB = subchondral bone.

In the simulations with layered and isotropic susceptibility distribution it was observed, that some magic angle anisotropy could exist in QSM even if the susceptibility was isotropic, at least if there was no signal available outside of the sample with layered susceptibility (Figure 7.5).

Study **I** also revealed that the QSM processing pathway may drastically affect results of QSM in cartilage (Figure 7.6). More specifically, it was observed that the background removal method plays a critical role in the successful QSM of articular cartilage, as some methods might be intolerant to the susceptibility difference

at the osteochondral junction, causing susceptibility distribution of cartilage to be exaggerated.
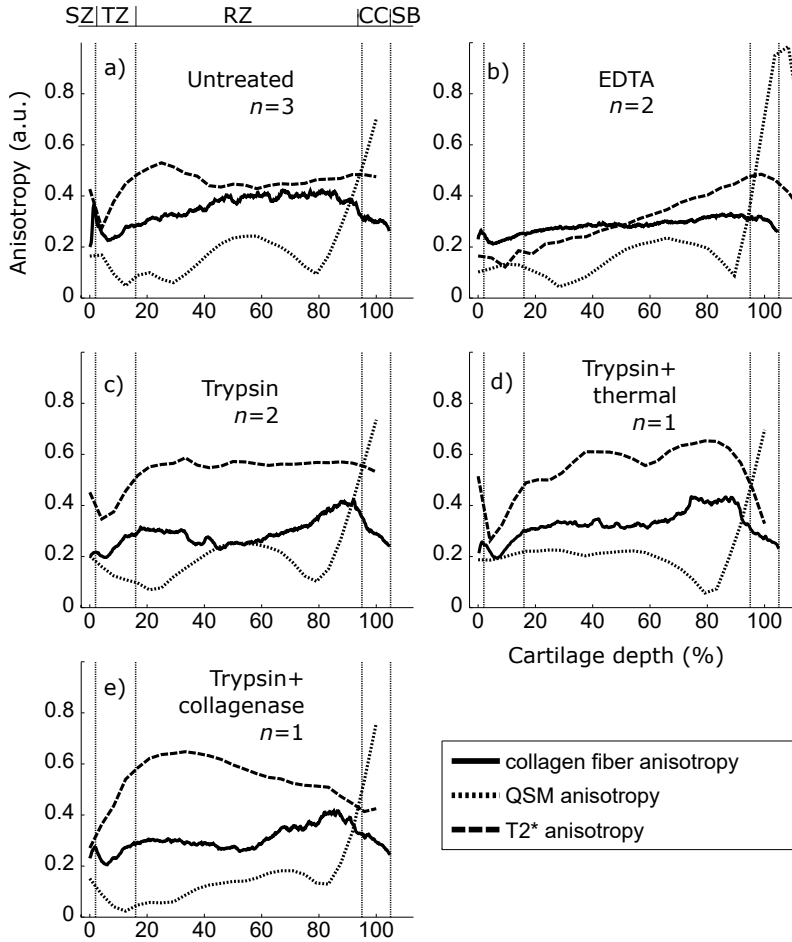
Figure 7.4: The anisotropy of collagen fiber network along with the anisotropies of apparent magnetic susceptibility and T_2^* relaxation time. The anisotropy of the susceptibility is markedly different from the others, as it is most evident at the osteochondral junction.

In study **II**, it was observed that experimental and control samples exhibited differences in susceptibility; at the central locations of the samples, differences between the susceptibility profiles of the experiment and control samples were statistically significant near to the lesions (Figure 7.7). At the distal and proximal measurement locations, the difference between the experiment and control samples was higher as one moved further away from the lesions (Figure 7.7). The depth profiles were flatter for the experimental group, most notably at central locations (Figure 7.7). However, while the depth-wise changes were reduced in OA, the spatial variation over the articular surface was increased (Figure 7.8), possibly due to focal defects in the sample or issues related to the QSM processing of thin samples.
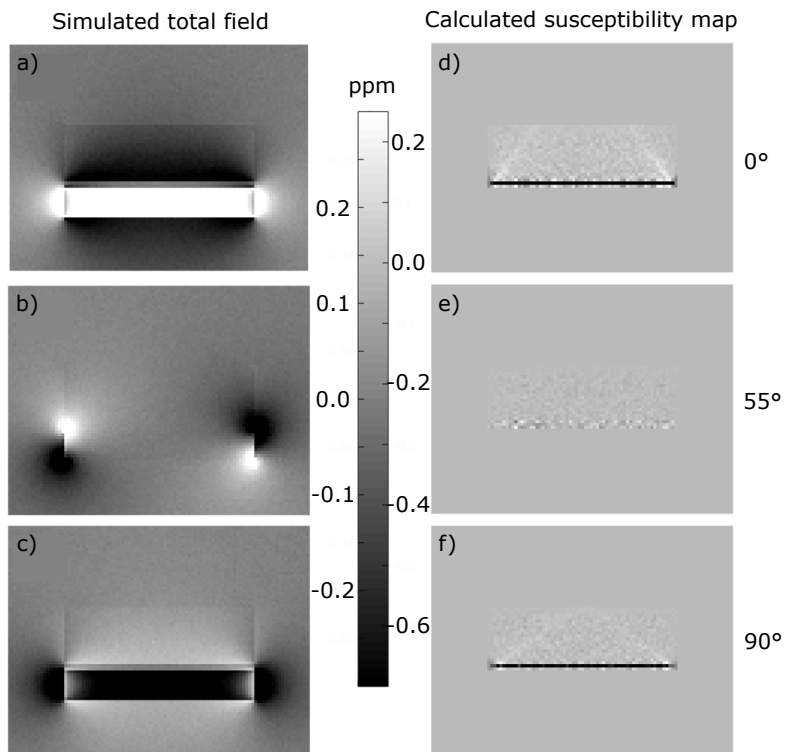
Figure 7.5: The results of QSM simulation in different orientations of the layered susceptibility distribution with respect to the main magnetic field. The layers seem to vanish at the 55° orientation.
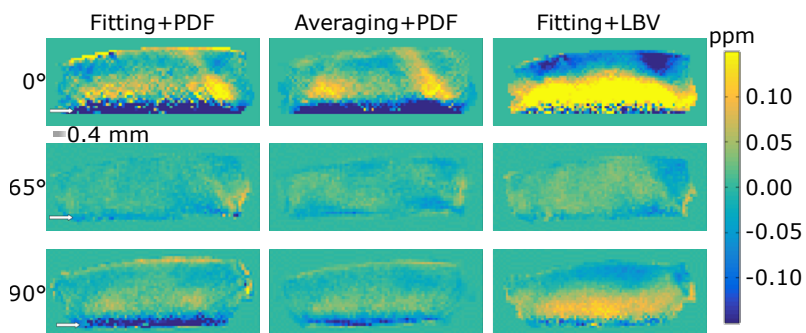
Figure 7.6: The QSM results from articular cartilage using different processing pathways. The use of LBV instead of PDF clearly affected the determined susceptibility distribution.
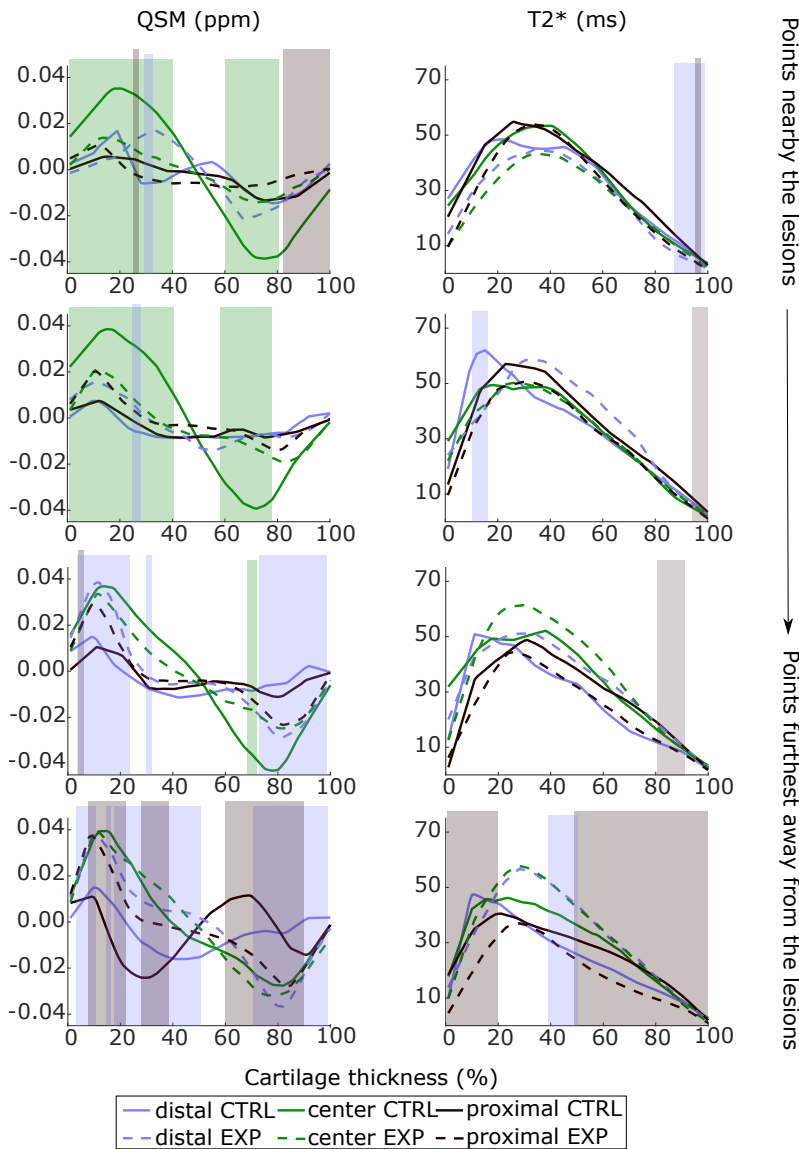
Figure 7.7: The depth-wise susceptibility and T_2^* profiles at different measurement points at the trochlear ridges of equine specimens. The difference between the experimental and control samples is statistically significant at the locations indicated by the shaded areas.

Furthermore, the direct correlation or the PLSR analysis did not reveal strong correlations between the susceptibility and any of the reference properties of articular cartilage. The highest correlations were found between the superficial susceptibility and collagen fiber angle in the direct correlation analysis and between the susceptibility and proteoglycan content in the PLSR analysis (Tables 7.1 and 7.2). In the PLSR analysis, it was beneficial to combine information from both QSM and T_2^*-relaxation time mapping, as this both increased the correlation and decreased the

error between the predicted and measured reference properties. The highest correlation between combined susceptibility and T_2^* data and the reference data was found between MRI and collagen fiber anisotropy, although also the correlations between MRI and proteoglycan content were relatively high (Tables 7.1 and 7.2). The correlations between MRI and the biomechanical properties were somewhat lower. This indicates that MRI is more sensitive towards tissue composition than its mechanical properties, which is rather to be expected.

7.3 T_2^* RELAXATION TIME MAPPING

In addition to QSM, also the T_2^* relaxation time was analysed in this study, as it was readily available from the same MRI data. Since T_2 (*sic.*) relaxation time mapping has been found to correlate with tissue degeneration, especially with changes in the collagen network in articular cartilage, the related T_2^* relaxation time was compared with QSM to evaluate QSM's potential benefits against other qMRI parameters.

In study **I**, it was noticed that T_2^* relaxation is more sensitive to detecting degradations when compared to QSM, although it was also found to be relatively insensitive (Figure 7.3). Furthermore, it was observed that T_2^* relaxation time anisotropy more closely resembled the collagen fiber anisotropy of articular cartilage measured with PLM (Figure 7.4). The anisotropy of the T_2^* relaxation time was not significantly affected by the degradations; only with the EDTA decalcification was the anisotropy clearly decreased (Figure 7.4). T_2^* relaxation time profiles displayed depth-wise contrast which is very similar when compared to the T_2 relaxation time mapping. The relaxation time was longest at the transitional layer of articular cartilage and then decreased rapidly towards the deep cartilage at $0°$ orientation with respect to the magnetic field. Near to the magic angle, the decrease from the transitional to the deep layer was found to be less intense (Figure 7.3).
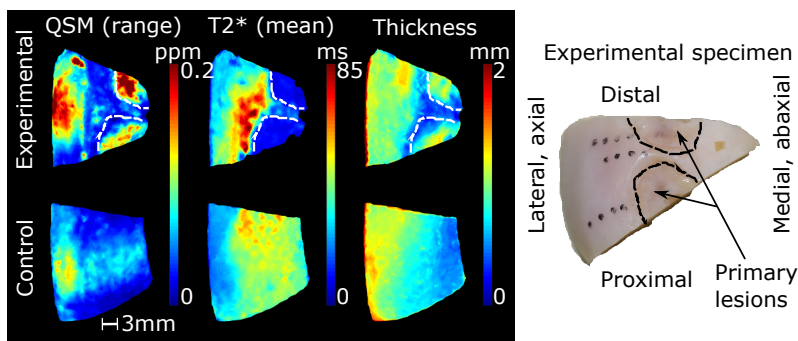
Figure 7.8: Surface maps of QSM and T_2^* relaxation time distributions in the equine samples. Cartilage thickness map (estimated from the MR intensity image) and a photograph of an experimental sample are also presented.

In study **II**, it was seen that T_2^* relaxation time did not vary much between the experimental and control samples, as significant differences between T_2^* relaxation times of the experimental and control samples were noted only at 1 out of 12 measurement locations (Figure 7.7). However, in PLSR analysis, T_2^* relaxation time mapping showed generally stronger correlation between the predicted and

measured reference data than QSM (Tables 7.1 and 7.2, Figure 7.9). The clearest correlation was seen between T_2^* relaxation time and the proteoglycan content as measured by optical density (Tables 7.1 and 7.2). In the direct correlation analysis, most of the correlation coefficients between the T_2^* relaxation time and the reference properties were low. The strongest correlation was found between T_2^* relaxation time and collagen fiber anisotropy (Tables 7.1 and 7.2).

Table 7.1: Spearman rank correlation coefficients between the MRI parameters and biomechanical properties and proteoglycan contents of articular cartilage in study **II**. The asterisk (*) indicates statistical significance ($p<0.05$).

	Equilibrium modulus (MPa)	Dynamic modulus (MPa)	Proteoglycan content (o.d.)	Superficial PG content (o.d.)
QSM	0.07	0.07	0.15*	0.16*
T_2^*	-0.35*	-0.33*	-0.26*	-0.23*
superficial QSM	0.29*	0.26*	0.34*	0.34*
superficial T_2^*	-0.08	-0.08	-0.10	-0.05
QSM (PLSR)	0.47*	0.41*	0.55*	0.51*
T_2^* (PLSR)	0.56*	0.52*	0.66*	0.57*
QSM & T_2^* (PLSR)	0.61*	0.61*	0.67*	0.67*

Table 7.2: Spearman rank correlation coefficients between the MRI parameters and collagen network properties of articular cartilage in study **II**. The asterisk (*) indicates statistical significance ($p<0.05$).

	Fiber angle (°)	Superficial fiber angle (°)	Anisotropy (a.u.)	Superficial anisotropy (a.u.)
QSM	0.24*	0.24*	0.03	-0.22*
T_2^*	-0.30*	-0.19*	-0.46*	-0.08
superficial QSM	0.40*	0.32*	0.26*	-0.16*
superficial T_2^*	-0.06	-0.06	-0.10	-0.03
QSM (PLSR)	0.44*	0.32*	0.47*	0.21*
T_2^* (PLSR)	0.49*	0.34*	0.63*	0.18*
QSM & T_2^* (PLSR)	0.61*	0.41*	0.68*	0.23*
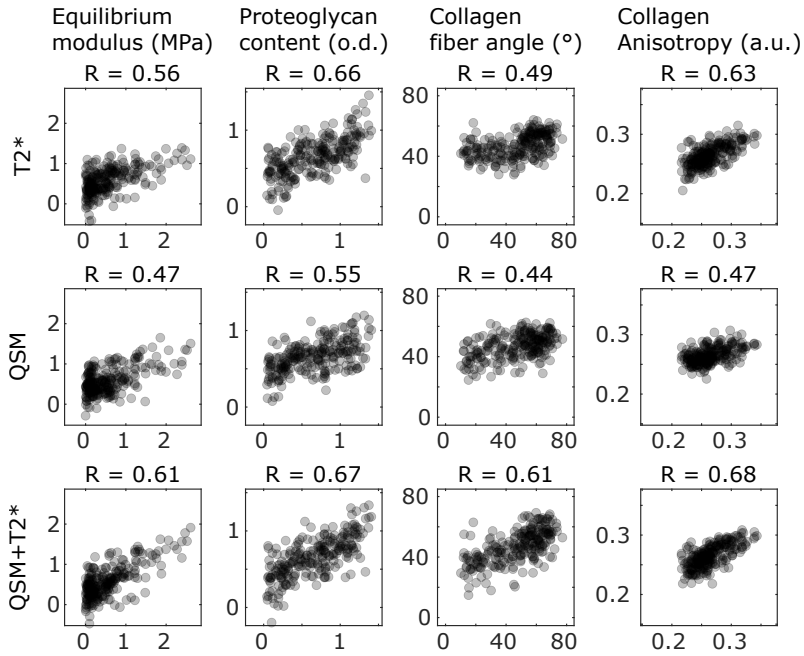
Figure 7.9: PLSR predictions of the reference properties from the MRI data.

7.4 SWIFT

In study **III**, SWIFT-MRI of the osteochondral samples was examined. The bright signal feature at the osteochondral junction was of special interest. The study showed that co-registration between μCT and MRI was possible, allowing a detailed analysis of signal locations in SWIFT MRI and μCT (Figure 6.3). The short-T_2^* images confirmed that the hyperintense SWIFT signal near to the osteochondral interface is mostly comprised of the signal from the short-T_2^* components, such as bound water or water whose relaxation time is decreased due to field differences (susceptibility effects) (Figure 7.10).

The co-registration and analysis of the profiles calculated from the MR- and μCT images showed that the hyperintense signal in SWIFT MRI is not located in the calcified cartilage, but instead it is observed in the deep noncalcified articular cartilage, above the calcified cartilage. This is evident, since the calcified cartilage has high signal in the μCT images as confirmed by the comparison between Masson's trichrome stained histological sections, demonstrating that the calcified cartilage is seen as bone by μCT (Figure 7.10). Furthermore, variations in the intensity of this signal were noted between the samples, hinting that the properties of the osteochondral unit may contribute to this signal (Figure 7.11 a and b). A further analysis using the bovine sample revealed that T_1-relaxation time gradually decreases towards the osteochondral interface (Figure 7.11 e). More interestingly, changing the receiver bandwidth in the imaging revealed that the hyperintense signal is blurred at narrower bandwidths (Figure 7.11 c and d).
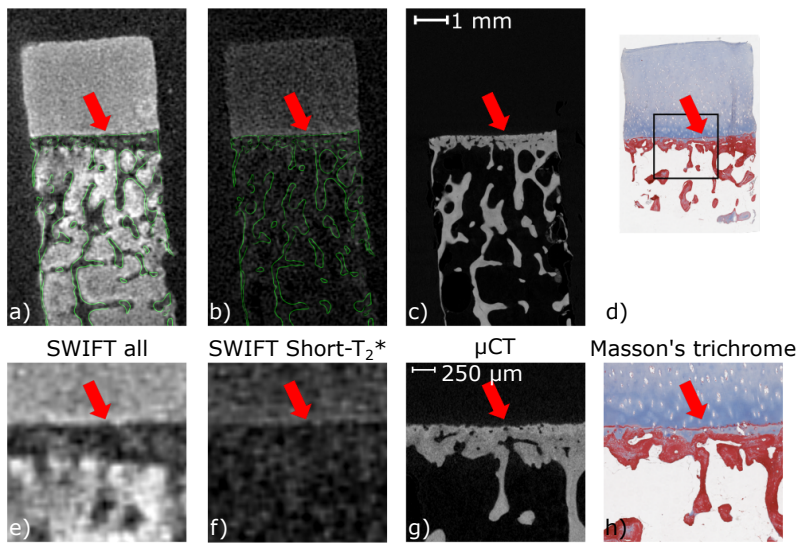
Figure 7.10: SWIFT images with all signals in-focus (a,e) and short-T_2^* signals only (b,f) compared with the μCT (c,g) and light microscopy (d,h) images of the same sample. The bright signal in SWIFT-MRI is above the calcified cartilage, which is seen in μCT image as bone.
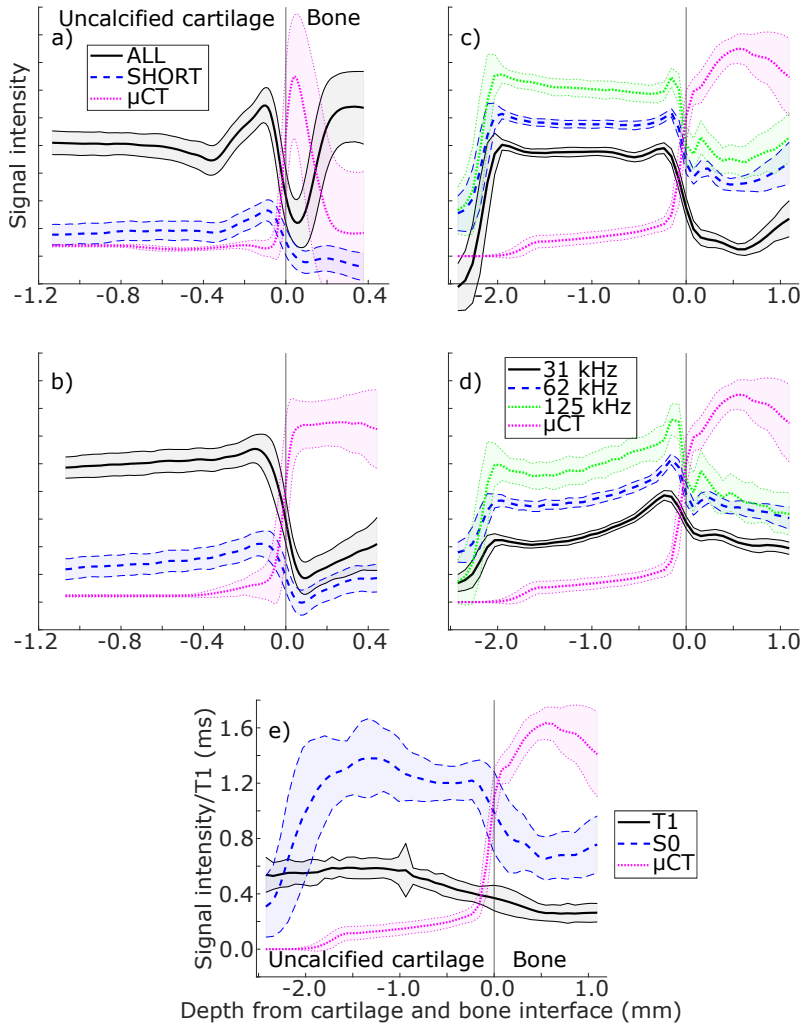
Figure 7.11: SWIFT and μCT profiles through different osteochondral samples. a) Human sample with high intensity at the osteochondral interface, b) human sample with markedly lower signal at the interface, c) bovine sample imaged with different bandwidths, all SWIFT signal, d) same as c but only with Short-T_2^* signals, and e) T_1 relaxation time profile from bovine sample (BW = 62.5 kHz). The shaded areas describe the standard deviation of the profile.

8 Discussion

New contrast mechanisms for MRI of articular cartilage are being continuously sought, since the current mechanisms do not yet provide sufficient information about the state of the cartilage or these techniques are difficult to use [12, 68, 115]. Thus, in this study, the potential of QSM and T_2^* in the assessment of articular cartilage properties was examined. Moreover, the hyperintense signal seen at the osteochondral junction using ultra-short echo time imaging methods, was examined using the SWIFT-sequence. More precisely, the study aimed to find a reliable processing pathway for QSM of articular cartilage in *ex vivo* setting and then to evaluate how the QSM-contrast in cartilage would be affected by changes in the structural properties of cartilage. The study also aimed to associate QSM and T_2^* relaxation time with changes in cartilage induced by post-traumatic osteoarthritis. Lastly, the hyperintense signal observed in SWIFT imaging of articular cartilage was precisely localized with the aid of μCT and the potential origins of that signal were evaluated.

8.1 QSM AND T_2^* RELAXATION TIME MAPPING

To sum up, the present QSM results from imaging of articular cartilage are somewhat nuanced: it seems that to some extent QSM *is* able to differentiate between healthy and osteoarthritic cartilage, but on the other hand QSM in cartilage does not seem to be clearly related to any of the studied *properties* of articular cartilage, such as its biomechanical properties or proteoglycan content. More specifically, the depth-wise contrast was almost unchanged between the different degradative treatments in study **I** and revealed only mild correlations with the tissue properties in study **II**. The determined anisotropy of QSM did not directly follow either the anisotropy or the fiber angle of the collagen network as observed by PLM. This was rather unexpected, since susceptibility tensor imaging has been successfully used in collagen fiber tracking of articular cartilage samples [87], although in that study, the fiber orientation was confirmed with atomic force microscopy, that did not allow imaging of the fiber orientation through the cartilage depth in one image. However, the effect of the anisotropy was strongest at the magic angle, as has been observed for other quantitative MRI parameters in articular cartilage [84]. However, the simulations showed that a specific layered sample geometry, such as is present in the structure of articular cartilage, can induce a similar apparent "anisotropy" in the QSM of the target. This is likely caused by the fact that at the magic angle orientation, the field differences are mostly generated outside the ROI.

On the positive side, combining QSM with the T_2^* relaxation time increased the predictive power of the PLSR-analysis in study **II**, indicating that since both parameters can be evaluated from the same measurement, the information from QSM should not be discarded. One curious observation was that background field removal method had a dramatic effect on the QSM results; this was not expected, as a rather similar performance between the different methods was found in a comprehensive review paper (assessing brain imaging) [58]. More specifically, LBV methods seemed to be intolerant towards the high susceptibility difference at the cartilage-

calcified cartilage boundary, causing a dramatic difference in the estimated susceptibility distribution. This can be explained by the different boundary conditions utilized in the methods [58] and the fact that in *ex vivo* imaging of osteochondral plugs, the boundary is always near the target tissue whereas in brains there are regions that are further from the boundaries.

When compared to the other studies on QSM of articular cartilage, it can be noted that the susceptibility contrast was different between our work and the study of Wei *et al.*, investigating the susceptibility contrast in articular cartilage [86]. In study **I**, the susceptibility fluctuated around zero throughout most of the cartilage, until there was a sudden decline in susceptibility towards the osteochondral interface, whereas in the study of Wei *et al.*, the susceptibility seemed to gradually decrease towards the interface [86]. However, the QSM contrast in study **II** was more reminiscent of the previous observation [86]. This difference between the observations reported in studies **I** and **II**, and in the literature might be explained by the fact that in study **I**, the cartilage samples were from bovine patellar cartilage, whereas the samples in study **II** were from equine trochlear ridges and samples of the previous studies were from porcine femoral condyles [86, 87]. It also seems that in another study conducted by Wei *et al.*, the cartilage samples were formalin fixed prior to the imaging [87] which might have altered the susceptibility contrast compared to the "fresh" samples that we utilized in studies **I** and **II**. This may have also affected the unexpected observations regarding the anisotropy of QSM in study **I**. Formalin fixation has been shown to significantly affect at least T_2 relaxation contrast and magnetization transfer effects in cartilage [116] and these effects might be expected also for QSM. The QSM of the knee joint has also been examined in the clinical setting, and although direct comparison between the *ex* and *in vivo* measurements is not possible, rather similar findings (flattening of depth-wise profile of QSM in osteoarthritic cartilage) have been reported [88].

T_2^*-relaxation time in cartilage appears to display many similarities with the T_2 relaxation, which is of course unsurprising, but also hints that the native susceptibility might not have a very important role in the MRI of articular cartilage, since susceptibility differences are one of the main factors causing differences between T_2^*- and T_2 relaxations. However, if even small susceptibility differences can be detected in articular cartilage, they might be valuable. Both T_2^*- and T_2 relaxations showed tri-layered depth-wise contrast, i.e. the T_2^* relaxation time is low near to the cartilage surface, then it becomes prolonged in the transitional zone of cartilage and decreases rapidly towards the osteochondral interface at $0°$ and $90°$ orientations with respect to the main magnetic field. Near to the magic angle, the T_2^* relaxation time increases throughout the cartilage depth, again similarly as the T_2 relaxation time. Consequently, the anisotropy of T_2^* relaxation is very similar to that of T_2-relaxation. Earlier, it has been suggested that the T_2 relaxation time mostly depends on the collagen network of the cartilage [93], but results from the PLSR-analysis suggest that also proteoglycan loss affects the T_2^*-relaxation.

PLSR-analysis was successfully applied in the study, and it was shown to have a moderate ability to predict the properties of cartilage based on the MRI data. One important finding was that while T_2^* was a better predictor than QSM when applied alone, adding both data to the analysis increased the predictive power. Moreover, it was noticed that the PLSR analysis (or a prediction based on it) yielded higher correlations between MRI data and cartilage properties than a direct correlation analysis. This suggests that the multivariate analysis represents a direction in which quantitative MRI of articular cartilage should be developed in the future, as also suggested

in earlier studies [13, 117, 118]. It was especially encouraging that correlations by PLSR-analysis were moderate between MRI and cartilage properties even though QSM and T_2^*-relaxation time mapping are not well-established methods in cartilage imaging.

8.2 SWIFT

The study with SWIFT-sequence showed that the hyperintense signal in the vicinity of the osteochondral interface was not located in the calcified cartilage but was instead in the deep uncalcified articular cartilage. However, this does not necessarily indicate that the hyperintense signal, or changes in it would not reflect the properties of the calcified cartilage, especially since the previous publications on the subject have already shown that the presence of calcified cartilage is needed to generate the signal [96, 99].

It was indeed also observed in this study that the signal was blurred with a lower receiver bandwidth, which indicates that the signal had slightly altered the Larmor frequency. The location of the highest intensity also changed slightly when imaging at the different bandwidths; the signal maxima shifted away from the bone-cartilage interface with lower receiver bandwidths. These observations indicate that whatever contributes to this signal may have a different susceptibility when compared to the more superficial, uncalcified parts of the cartilage. In line with this finding, in study **I**, a major decrease was observed in the susceptibility values towards the osteochondral junction. It has also been reported elsewhere that cortical bone has a markedly lower susceptibility than soft tissues [119]. Taken together, this hints that the signal may be at least partially generated by a signal mislocation due to the field inhomogeneities around the interface.

Another observation was that the T_1 relaxation was faster near to the interface, and although the change in T_1 relaxation time was not as intense as the observed hyperintense signal would require, it did indicate that T_1 relaxation plays a partial role in the generation of the bright signal in UTE imaging of the osteochondral junction. A faster T_1 relaxation towards deep cartilage has also been observed in an earlier study employing SWIFT using variable flip angles [49]. One possible explanation for the signal would be extremely high spin density near to the interface, but this proposal is not supported by the fact that the amount of water in the cartilage is generally highest near the cartilage surface and decreases towards the deeper layers [2].

All in all, the hyperintense signal at the osteochondral interface may be useful for evaluating the status of articular cartilage and also of the osteochondral junction. However, further studies will be required to clarify which properties of the osteochondral junction generate the signal and how the changes in these properties affect the obtained signal.

8.3 LIMITATIONS

The studies comprising this thesis have a few limitations. Firstly, in studies **I** and **II**, the susceptibility was not referenced with an external reference and since all of the useful signal was from the cartilage itself, it was not possible to detect base level changes in the susceptibility, e.g. it is not possible to determine whether the susceptibility in the trypsin-treated samples was truly similar as compared to the

intact samples or if there had been a complete base level shift, but a similar depth-wise contrast. The possible undetected base level shift could have also affected the results regarding the observed anisotropy of the susceptibility. In study **II**, this was not as great a concern since the samples were larger and spatial differences could be evaluated. However, it seems most unlikely that including the susceptibility reference in the data would have radically changed the interpretation of the results.

Another method-related limitation is that the applied echo times were some-what short considering accurate T_2^*-relaxation time mapping near to the cartilage surface. This may have led to an over-estimation of the longest (>100ms) T_2^* re-laxation components, but as significant correlations were found between T_2^* and cartilage properties also with this setting, this limitation is not very critical.

A third limitation is the low number of samples in studies **I** and **III**, although the studies were more methodological in their approaches; in study **III**, the obser-vations about the hyperintense signal were so clear that the sample size would not be expected to have any effect on the results.

Another limitation concerning all of the studies included in this thesis is that they were all performed using *ex vivo* samples, and thus the results cannot necessarily be very well generalized to clinical imaging. For example, PLSR-analysis is likely to be more accurate with a higher resolution through the cartilage depth, as is possible with *ex vivo* imaging. On the other hand, the referencing issue with QSM can be almost completely resolved in the clinical setting, as the susceptibilities could be referenced with other tissues in addition to cartilage.

Imaging times in all studies were also unacceptably long from a clinical point of view, but because acquisition speed was not a priority here, speed-up methods, such as parallel imaging or compressed sensing, were not considered. Thus, there should be room for significantly reducing the imaging times. In fact, very long repetition times in QSM sequences were also deliberately used to limit the gradient duty cycle.

8.4 CONCLUSIONS

In conclusion, native QSM may have its niche uses in MR-imaging of the osteo-chondral unit but it does not seem to be the method of choice in most situations. However, observations with the SWIFT sequence suggest, that if we could measure the susceptibility nearby to the osteochondral interface reliably and with high res-olution, it would likely provide new insights into the status of the osteochondral interface. T_2^*-relaxation time was revealed to yield rather similar results from car-tilage when compared to the more widely studied T_2 relaxation. This information might be useful, since gradient echo -based sequences are generally considereably faster than spin echo sequences that are often used in the T_2-relaxation time mea-surements. The most important observation emerging from the SWIFT-studies was that the bright signal feature that has been observed in the vicinity of the osteo-chondral junction is not located in the calcified cartilage, indicating that it cannot be directly utilized in studies concerning calcified cartilage.

8.5 FUTURE WORK

The findings in this thesis pave the way for future works regarding the topics of this thesis. Firstly, even though the results using QSM were not completely encour-aging, the possibilities of using QSM for imaging articular cartilage using contrast

agents could be evaluated in the future. Secondly, the results of study **II** indicate that multivariate analysis might be one way to progress regarding the OA diagnostics using quantitative MRI. For example, a similar analysis using *e.g.* $T_{1\rho}$ relaxation time measurement should be conducted. Lastly, as only the localization of the hyperintense signal was examined in study **III**, a larger trial probing this signal by exploiting quantitative MRI should be conducted to evaluate whether any tissue changes caused by OA are evident from the quantitative properties of this signal.

BIBLIOGRAPHY

[1] J. A. Buckwalter and J. Martin, "Degenerative joint disease.," in *Clinical symposia (Summit, NJ: 1957)*, Vol. 47 (1995), pp. 1–32.

[2] J. Buckwalter and H. Mankin, "Instructional Course Lectures, The American Society of Orthopaedic Surgeons – Articular Cartilage. Part I: Tissue Design and Chondrocyte-Matrix Interactions," *The Journal of Bone and Joint Surgery* **79**, 600–611 (1997).

[3] Y. Zhang and J. M. Jordan, "Epidemiology of osteoarthritis," *Clinics in geriatric medicine* **26**, 355–369 (2010).

[4] J. Buckwalter and H. Mankin, "Instructional Course Lectures, The American Society of Orthopaedic Surgeons – Articular Cartilage. Part II: Degeneration and Osteoarthrosis, Repair, Regeneration, and Transplantation," *The Journal of Bone and Joint Surgery* **79**, 612–632 (1997).

[5] M. Goldring and S. Goldring, "Articular cartilage and subchondral bone in the pathogenesis of osteoarthritis," *annals of New York Academy of Sciences* **1192**, 230–237 (2010).

[6] M. Heliövaara, P. Slätis, and P. Paavolainen, "Nivelrikon esiintyvyys ja kustannukset," *Duodecim* **124**, 1869–1874 (2008).

[7] W. Oo, S.-C. Yu, M. Daniel, and D. Hunter, "Disease-modifying drugs in osteoarthritis: current understanding and future therapeutics," *Expert opinion on emerging drugs* **23**, 331–347 (2018).

[8] C. Chu, A. Williams, C. Coyle, and M. Bowers, "Early diagnosis to enable early treatment of pre-osteoarthritis," *Arthritis Researh & Therapy* **14**, 212 (2012).

[9] F. W. Roemer, M. D. Crema, S. Trattnig, and A. Guermazi, "Advances in imaging of osteoarthritis and cartilage," *Radiology* **260**, 332–354 (2011).

[10] M. Schreiner, Zbýň, B. Schmitt, M. Weber, S. Domayer, R. Windhager, S. Trattnig, and V. Mlynárik, "Reproducibility and regional variations of an improved gagCEST protocol for the in vivo evaluation of knee cartilage at 7 T," *Magnetic Resonance Materials in Physics, Biology and Medicine* **29**, 513–521 (2016).

[11] A. Guermazi, H. Alizai, M. Crema, S. Trattnig, R. Regatte, and F. Roemer, "Compositional MRI techniques for evaluation of cartilage degeneration in osteoarthritis," *Osteoarthritis and cartilage* **23**, 1639–1653 (2015).

[12] S. J. Matzat, F. Kogan, G. W. Fong, and G. E. Gold, "Imaging strategies for assessing cartilage composition in osteoarthritis," *Current rheumatology reports* **16**, 462 (2014).

[13] X. Li and S. Majumdar, "Quantitative MRI of articular cartilage and its clinical applications," *Journal of Magnetic Resonance Imaging* **38**, 991–1008 (2013).

[14] J. Marques and R. Bowtell, "Application of a Fourier-based method for rapid calculation of field inhomogeneity due to spatial variation of magnetic susceptibility," *Concepts in Magnetic Resonance Part B: Magnetic Resonance Engineering* **25**, 65–78 (2005).

[15] D. Idiyatullin, C. Corum, J. Park, and M. Garwood, "Fast and quiet MRI using a swept radiofrequency," *J Magn Reson* **181**, 342–9 (2006).

[16] P. Gatehouse, R. Thomas, M. Robson, G. Hamilton, A. Herlihy, and G. Bydder, "Magnetic resonance imaging of the knee with ultrashort TE pulse sequences," *Magn Reson Imaging* **22**, 1061–7 (2004).

[17] J. Du, M. Carl, W. Bae, S. Statum, E. Chang, G. Bydder, and C. B. C., "Dual inversion recovery ultrashort echo time (DIR-UTE) imaging and quantification of the zone of calcified cartilage (ZCC)," *Osteoarthritis and cartilage* **21**, 77–85 (2013).

[18] A. J. Sophia Fox, A. Bedi, and S. A. Rodeo, "The basic science of articular cartilage: structure, composition, and function," *Sports health* **1**, 461–468 (2009).

[19] C. D. Hoemann, C.-H. Lafantaisie-Favreau, V. Lascau-Coman, G. Chen, and J. Guzmán-Morales, "The cartilage-bone interface," *The journal of knee surgery* **25**, 085–098 (2012).

[20] V. C. Mow, A. Ratcliffe, and A. R. Poole, "Cartilage and diarthrodial joints as paradigms for hierarchical materials and structures," *Biomaterials* **13**, 67–97 (1992).

[21] D. R. Eyre, M. A. Weis, and J.-J. Wu, "Articular cartilage collagen: an irreplaceable framework," *Eur Cell Mater* **12**, 57–63 (2006).

[22] M. D. Shoulders and R. T. Raines, "Collagen structure and stability," *Annual review of biochemistry* **78**, 929–958 (2009).

[23] V. Mow, "Fundamentals of articular cartilage and meniscus biomechanics," *Articular cartilage and knee joint function* 1–18 (1990).

[24] P. J. Roughley and J. S. Mort, "The role of aggrecan in normal and osteoarthritic cartilage," *Journal of experimental orthopaedics* **1**, 1–11 (2014).

[25] H. Muir, "The chondrocyte, architect of cartilage. Biomechanics, structure, function and molecular biology of cartilage matrix macromolecules," *Bioessays* **17**, 1039–1048 (1995).

[26] V. C. Mow, "Structure and function of articular cartilage and meniscus," *Basic orthopaedic biomechanics* 31–58 (1997).

[27] A. Maroudas and R. Schneiderman, ""Free" and "exchangeable" or "trapped" and "non-exchangeable" water in cartilage," *Journal of orthopaedic research* **5**, 133–138 (1987).

[28] M. Keeney and A. Pandit, "The osteochondral junction and its repair via bi-phasic tissue engineering scaffolds," *Tissue Engineering Part B: Reviews* **15**, 55–73 (2009).

[29] S. Suri and D. Walsh, "Osteochondral alterations in osteoarthritis," *Bone* **51**, 204–211 (2012).

[30] J. Buckwalter and T. Brown, "Joint injury, repair, and remodeling: roles in post-traumatic osteoarthritis," *Clinical Orthopaedics and Related Research®* **423**, 7–16 (2004).

[31] A. Thambyah and N. Broom, "On how degeneration influences load-bearing in the cartilage–bone system: a microstructural and micromechanical study," *Osteoarthritis and Cartilage* **15**, 1410–1423 (2007).

[32] H. Imhof, M. Breitenseher, F. Kainberger, and S. Trattnig, "Degenerative joint disease: cartilage or vascular disease?," *Skeletal radiology* **26**, 398–403 (1997).

[33] D. Burr and M. Gallant, "Bone remodelling in osteoarthritis," *Nature Reviews Rheumatology* **8**, 665 (2012).

[34] A. Thambyah and N. Broom, "How subtle structural changes associated with maturity and mild degeneration influence the impact-induced failure modes of cartilage-on-bone," *Clinical Biomechanics* **25**, 737–744 (2010).

[35] C. Nguyen, M.-M. Lefevre-Colau, S. Poiraudeau, and F. Rannou, "Rehabilitation (exercise and strength training) and osteoarthritis: A critical narrative review," *Annals of physical and rehabilitation medicine* **59**, 190–195 (2016).

[36] R. W. Brown, Y.-C. N. Cheng, E. M. Haacke, M. R. Thompson, and R. Venkatesan, *Magnetic resonance imaging: physical principles and sequence design* (John Wiley & Sons, 2014).

[37] M. A. Brown and R. C. Semelka, *MRI: basic principles and applications* (John Wiley & Sons, 2011).

[38] D. W. McRobbie, E. A. Moore, M. J. Graves, and M. R. Prince, *MRI from Picture to Proton* (Cambridge university press, 2017).

[39] M. A. Bernstein, K. F. King, and X. J. Zhou, *Handbook of MRI pulse sequences* (Elsevier, 2004).

[40] M. H. Levitt, *Spin dynamics: basics of nuclear magnetic resonance* (John Wiley & Sons, 2001).

[41] M. D. Robson, P. D. Gatehouse, M. Bydder, and G. M. Bydder, "Magnetic resonance: an introduction to ultrashort TE (UTE) imaging," *Journal of computer assisted tomography* **27**, 825–846 (2003).

[42] M. Garwood, "MRI of fast-relaxing spins," *Journal of magnetic resonance* **229**, 49–54 (2013).

[43] J. Du, M. Carl, M. Bydder, A. Takahashi, C. B. Chung, and G. M. Bydder, "Qualitative and quantitative ultrashort echo time (UTE) imaging of cortical bone," *Journal of Magnetic Resonance* **207**, 304–311 (2010).

[44] M. Weiger and K. Pruessmann, "MRI with zero echo time," *eMagRes* (2007).

[45] D. Idiyatullin, C. Corum, S. Moeller, H. Prasad, M. Garwood, and D. Nixdorf, "Dental magnetic resonance imaging: making the invisible visible," *J Endod* **37**, 745–52 (2011).

[46] M. Weiger, K. P. Pruessmann, A.-K. Bracher, S. Köhler, V. Lehmann, U. Wolfram, F. Hennel, and V. Rasche, "High-resolution ZTE imaging of human teeth," *NMR in Biomedicine* **25**, 1144–1151 (2012).

[47] R. R. Ernst, "Magnetic resonance with stochastic excitation," *Journal of Magnetic Resonance (1969)* **3**, 10–27 (1970).

[48] L. Wang, C. A. Corum, D. Idiyatullin, M. Garwood, and Q. Zhao, "T1 estimation for aqueous iron oxide nanoparticle suspensions using a variable flip angle SWIFT sequence," *Magnetic resonance in medicine* **70**, 341–347 (2013).

[49] M. J. Nissi, L. J. Lehto, C. A. Corum, D. Idiyatullin, J. M. Ellermann, O. H. Gröhn, and M. T. Nieminen, "Measurement of T1 relaxation time of osteochondral specimens using VFA-SWIFT," *Magnetic resonance in medicine* **74**, 175–184 (2015).

[50] F. Schweser, A. Deistung, and J. Reichenbach, "Foundations of MRI phase imaging and processing for Quantitative Susceptibility Mapping (QSM)," *Zeitschrift für Medizinische Physik* (2015).

[51] Y. Wang and T. Liu, "Quantitative susceptibility mapping (QSM): Decoding MRI data for a tissue magnetic biomarker," *Magnetic Resonance in Medicine* **73**, 82–101 (2015).

[52] T. Liu, C. Wisnieff, M. Lou, W. Chen, P. Spincemaille, and Y. Wang, "Nonlinear formulation of the magnetic field to source relationship for robust quantitative susceptibility mapping," *Magnetic Resonance in Medicine* **69**, 467–476 (2013).

[53] B. Wu, W. Li, A. V. Avram, S.-M. Gho, and C. Liu, "Fast and tissue-optimized mapping of magnetic susceptibility and T2* with multi-echo and multi-shot spirals," *Neuroimage* **59**, 297–305 (2012).

[54] M. Schofield and Y. Zhu, "Fast phase unwrapping algorithm for interferometric applications," *Optics Letters* **28**, 3 (2004).

[55] K. Zhou, M. Zaitsev, and S. Bao, "Reliable two-dimensional phase unwrapping method using region growing and local linear estimation," *Magnetic Resonance in Medicine: An Official Journal of the International Society for Magnetic Resonance in Medicine* **62**, 1085–1090 (2009).

[56] S. Witoszynskyj, A. Rauscher, J. R. Reichenbach, and M. Barth, "Phase unwrapping of MR images using ΦUN–A fast and robust region growing algorithm," *Medical image analysis* **13**, 257–268 (2009).

[57] M. Hÿtch, E. Snoeck, and R. Kilaas, "Quantitative measurement of displacement and strain fields from HREM micrographs," *Ultramicroscopy* **74**, 131–146 (1998).

[58] F. Schweser, S. Robinson, L. Rochefort, W. Li, and K. Bredies, "An illustrated comparison of processing methods for phase MRI and QSM: removal of background field contributions from sources outside the region of interest," *NMR in Biomedicine* **30** (2017).

[59] T. Liu, I. Khalidov, L. de Rochefort, P. Spincemaille, J. Liu, A. Tsiouris, and Y. Wang, "A novel background field removal method for MRI using projection onto dipole fields (PDF)," *NMR in Biomedicine* **24**, 1129–1136 (2011).

[60] F. Schweser, A. Deistung, B. Lehr, and J. Reichenbach, "Quantitative imaging of intrinsic magnetic tissue properties using MRI signal phase: an approach to in vivo brain iron metabolism?," *Neuroimage* **54**, 2789–807 (2011).

[61] D. Zhou, T. Liu, P. Spincemaille, and Y. Wang, "Background field removal by solving the Laplacian boundary value problem," *NMR in Biomedicine* **27**, 312–319 (2014).

[62] C. Langkammer, F. Schweser, C. Kames, X. Li, L. Guo, C. Milovic, J. Kim, H. Wei, K. Bredies, S. Buch, Y. Guo, Z. Liu, J. Meineke, A. Rauscher, J. Marques, and B. Bilgic, "Quantitative Susceptibility Mapping: Report from the 2016 Reconstruction Challenge," *Magnetic Resonance in Medicine* **in press** (2017).

[63] K. Shmueli, J. de Zwart, P. van Gelderen, T. Li, S. Dodd, and J. Duyn, "Magnetic susceptibility mapping of brain tissue in vivo using MRI phase data," *Magnetic Resonance in Medicine* **62**, 1510–22 (2009).

[64] F. Schweser, A. Deistung, K. Sommer, and J. Reichenbach, "Toward online reconstruction of quantitative susceptibility maps: superfast dipole inversion," *Magnetic Resonance in Medicine* **69**, 1582–94 (2013).

[65] W. Li, A. V. Avram, B. Wu, X. Xiao, and C. Liu, "Integrated Laplacian-based phase unwrapping and background phase removal for quantitative susceptibility mapping," *NMR in Biomedicine* **27**, 219–227 (2014).

[66] Z. Liu, Y. Kee, D. Zhou, Y. Wang, and P. Spincemaille, "Preconditioned total field inversion (TFI) method for quantitative susceptibility mapping," *Magnetic Resonance in Medicine* (2016).

[67] P. B. Roemer, W. A. Edelstein, C. E. Hayes, S. P. Souza, and O. M. Mueller, "The NMR phased array," *Magnetic resonance in medicine* **16**, 192–225 (1990).

[68] M. Nieminen, V. Casula, M. Nevalainen, and S. Saarakkala, "Osteoarthritis year in review 2018: imaging," *Osteoarthritis and cartilage* **27**, 401–411 (2019).

[69] S. J. Matzat, J. van Tiel, G. E. Gold, and E. H. Oei, "Quantitative MRI techniques of cartilage composition," *Quantitative imaging in medicine and surgery* **3**, 162 (2013).

[70] D. J. Hunter, A. Guermazi, G. H. Lo, A. J. Grainger, P. G. Conaghan, R. M. Boudreau, and F. W. Roemer, "Evolution of semi-quantitative whole joint assessment of knee OA: MOAKS (MRI Osteoarthritis Knee Score)," *Osteoarthritis and Cartilage* **19**, 990–1002 (2011).

[71] L. Menashe, K. Hirko, E. Losina, M. Kloppenburg, W. Zhang, L. Li, and D. Hunter, "The diagnostic performance of MRI in osteoarthritis: a systematic review and meta-analysis," *Osteoarthritis and Cartilage* **20**, 13–21 (2012).

[72] M. Nissi, J. Rieppo, J. Töyräs, M. Laasanen, I. Kiviranta, M. Nieminen, and J. Jurvelin, "Estimation of mechanical properties of articular cartilage with MRI–dGEMRIC, T2 and T1 imaging in different species with variable stages of maturation," *Osteoarthritis and Cartilage* **15**, 1141–1148 (2007).

[73] Y. Xia, N. Wang, J. Lee, and F. Badar, "Strain-dependent T1 relaxation profiles in articular cartilage by MRI at microscopic resolutions," *Magnetic resonance in medicine* **65**, 1733–1737 (2011).

[74] J. Rautiainen, M. Nissi, E.-N. Salo, V. Tiitu, M. Finnilä, O.-M. Aho, S. Saarakkala, P. Lehenkari, J. Ellermann, and M. T. Nieminen, "Multiparametric MRI assessment of human articular cartilage degeneration: Correlation with quantitative histology and mechanical properties," *Magnetic Resonance in Medicine* (2014).

[75] T. J. Mosher and B. J. Dardzinski, "Cartilage MRI T2 relaxation time mapping: overview and applications," in *Seminars in musculoskeletal radiology*, Vol. 8 (Copyright© 2004 by Thieme Medical Publishers, Inc., 333 Seventh Avenue, New . . . , 2004), pp. 355–368.

[76] U. Duvvuri, R. Reddy, S. D. Patel, J. H. Kaufman, J. B. Kneeland, and J. S. Leigh, "T1ρ-relaxation in articular cartilage: effects of enzymatic degradation," *Magnetic resonance in medicine* **38**, 863–867 (1997).

[77] A. Bashir, M. L. Gray, and D. Burstein, "Gd-DTPA2- as a measure of cartilage degradation," *Magnetic resonance in medicine* **36**, 665–673 (1996).

[78] C. J. Tiderius, L. E. Olsson, P. Leander, O. Ekberg, and L. Dahlberg, "Delayed gadolinium-enhanced MRI of cartilage (dGEMRIC) in early knee osteoarthritis," *Magnetic Resonance in Medicine: An Official Journal of the International Society for Magnetic Resonance in Medicine* **49**, 488–492 (2003).

[79] E. Lammentausta, P. Kiviranta, M. Nissi, M. Laasanen, I. Kiviranta, M. Nieminen, and J. Jurvelin, "T2 relaxation time and delayed gadolinium-enhanced MRI of cartilage (dGEMRIC) of human patellar cartilage at 1.5 T and 9.4 T: Relationships with tissue mechanical properties," *Journal of orthopaedic research* **24**, 366–374 (2006).

[80] V. Mlynárik, I. Sulzbacher, M. Bittšanskỳ, R. Fuiko, and S. Trattnig, "Investigation of apparent diffusion constant as an indicator of early degenerative disease in articular cartilage," *Journal of Magnetic Resonance Imaging: An Official Journal of the International Society for Magnetic Resonance in Medicine* **17**, 440–444 (2003).

[81] J. G. Raya, A. Horng, O. Dietrich, S. Krasnokutsky, L. S. Beltran, P. Storey, M. F. Reiser, M. P. Recht, D. K. Sodickson, and C. Glaser, "Articular cartilage: in vivo diffusion-tensor imaging," *Radiology* **262**, 550–559 (2012).

[82] W. Ling, R. R. Regatte, G. Navon, and A. Jerschow, "Assessment of gly-cosaminoglycan concentration in vivo by chemical exchange-dependent satu-ration transfer (gagCEST)," *Proceedings of the National Academy of Sciences* **105**, 2266–2270 (2008).

[83] Zbýň, V. Mlynárik, V. Juras, P. Szomolanyi, and S. Trattnig, "Evaluation of cartilage repair and osteoarthritis with sodium MRI," *NMR in Biomedicine* **29**, 206–215 (2016).

[84] N. Hänninen, J. Rautiainen, L. Rieppo, S. Saarakkala, and M. Nissi, "Orienta-tion anisotropy of quantitative MRI relaxation parameters in ordered tissue," *Scientific Reports* **7** (2017).

[85] Y. Xia, "Magic-angle effect in magnetic resonance imaging of articular carti-lage: a review," *Investigative radiology* **35**, 602–621 (2000).

[86] H. Wei, R. Dibb, K. Decker, N. Wang, Y. Zhang, X. Zong, W. Lin, D. Nissman, and C. Liu, "Investigating magnetic susceptibility of human knee joint at 7 Tesla," *Magnetic resonance in medicine* **78**, 1933–1943 (2017).

[87] H. Wei, E. Gibbs, P. Zhao, N. Wang, G. Cofer, Y. Zhang, G. Johnson, and C. Liu, "Susceptibility tensor imaging and tractography of collagen fibrils in the articular cartilage," *Magn Reson Med* **78**, 1683–1690 (2017).

[88] H. Wei, H. Lin, L. Qin, S. Cao, Y. Zhang, N. He, W. Chen, F. Yan, and C. Liu, "Quantitative susceptibility mapping of articular cartilage in patients with os-teoarthritis at 3T," *Journal of Magnetic Resonance Imaging* (2018).

[89] M. Nissi, F. Toth, L. Wang, C. Carlson, and J. Ellermann, "Improved Visual-ization of Cartilage Canals Using Quantitative Susceptibility Mapping," *PLoS One* **10**, e0132167 (2015).

[90] B. Dymerska, K. Bohndorf, P. Schennach, A. Rauscher, S. Trattnig, and S. Robinson, "In vivo phase imaging of human epiphyseal cartilage at 7 T," *Magnetic resonance in medicine* **79**, 2149–2155 (2018).

[91] F. Tóth, C. Johnson, B. Mills, M. Nissi, O. Nykänen, J. Ellermann, K. Ludwig, M. Tompkins, and C. Carlson, "Evaluation of the Suitability of Miniature Pigs as an Animal Model of Juvenile Osteochondritis Dissecans," *Journal of Orthopaedic Research®* (2019).

[92] C. Liu, "Susceptibility tensor imaging," *Magnetic resonance in medicine* **63**, 1471–1477 (2010).

[93] M. Nieminen, J. Rieppo, J. Töyräs, J. Hakumäki, J. Silvennoinen, M. Hyttinen, H. Helminen, and J. S. Jurvelin, "T2 relaxation reveals spatial collagen archi-tecture in articular cartilage: a comparative quantitative MRI and polarized light microscopic study," *Magnetic Resonance in Medicine: An Official Journal of the International Society for Magnetic Resonance in Medicine* **46**, 487–493 (2001).

[94] T. C. Mamisch, T. Hughes, T. J. Mosher, C. Mueller, S. Trattnig, C. Boesch, and G. H. Welsch, "T2 star relaxation times for assessment of articular cartilage at 3 T: a feasibility study," *Skeletal radiology* **41**, 287–292 (2012).

[95] A. Williams, Y. Qian, D. Bear, and C. R. Chu, "Assessing degeneration of human articular cartilage with ultra-short echo time (UTE) T2* mapping," *Osteoarthritis and cartilage* **18**, 539–546 (2010).

[96] W. Bae, J. Dwek, R. Znamirowski, S. Statum, J. Hermida, D. D'Lima, R. Sah, J. Du, and C. Chung, "Ultrashort Echo Time MR Imaging of Osteochondral Junction of the Knee at 3 T: Identification of Anatomic Structures Contributing to Signal Intensity 1," *Radiology* **254**, 837–845 (2010).

[97] C. R. Chu, A. A. Williams, R. V. West, Y. Qian, F. H. Fu, B. H. Do, and S. Bruno, "Quantitative magnetic resonance imaging UTE-T2* mapping of cartilage and meniscus healing after anatomic anterior cruciate ligament reconstruction," *The American journal of sports medicine* **42**, 1847–1856 (2014).

[98] M. F. Koff, P. Shah, S. Pownder, B. Romero, R. Williams, S. Gilbert, S. Maher, L. A. Fortier, S. A. Rodeo, and H. G. Potter, "Correlation of meniscal T2* with multiphoton microscopy, and change of articular cartilage T2 in an ovine model of meniscal repair," *Osteoarthritis and cartilage* **21**, 1083–1091 (2013).

[99] W. Bae, R. Biswas, K. Chen, E. Chang, and C. Chung, "UTE MRI of the Osteochondral Junction," *Curr Radiol Rep* **2**, 35 (2014).

[100] J. Mackay, S. Low, G. Houston, and A. Toms, "Ultrashort TE evaluation of the osteochondral junction in vivo: a feasibility study," *The British journal of radiology* **89**, 20150493 (2016).

[101] M. A. Finnilä, J. Thevenot, O.-M. Aho, V. Tiitu, J. Rautiainen, S. Kauppinen, M. T. Nieminen, K. Pritzker, M. Valkealahti, P. Lehenkari, et al., "Association between subchondral bone structure and osteoarthritis histopathological grade," *Journal of Orthopaedic Research* **35**, 785–792 (2017).

[102] I. Mancini, F. Bragance, H. Brommer, J. Visser, J. Malda, and P. van Weeren, "Objective gait analysis as a tool to improve longitudinal monitoring of long-term large animal studies into cartilage repair," in *13th World Congress of ICRS, Sorrento, Italy* (2016).

[103] J. Sarin, N. te Moller, I. Mancini, H. Brommer, J. Visser, J. Malda, P. van Weeren, I. Afara, and J. Töyräs, "Arthroscopic near infrared spectroscopy enables simultaneous quantitative evaluation of articular cartilage and subchondral bone in vivo," *Scientific Reports* **8**, 13409 (2018).

[104] J. K. Sarin, O. Nykänen, V. Tiitu, I. A. Mancini, H. Brommer, J. Visser, J. Malda, P. R. van Weeren, I. O. Afara, and J. Töyräs, "Arthroscopic Determination of Cartilage Proteoglycan Content and Collagen Network Structure with Near-Infrared Spectroscopy," *Annals of biomedical engineering* **47**, 1815–1826 (2019).

[105] R. Delaine-Smith, S. Burney, F. Balkwill, and M. Knight, "Experimental validation of a flat punch indentation methodology calibrated against unconfined compression tests for determination of soft tissue biomechanics," *Journal of the mechanical behavior of biomedical materials* **60**, 401–415 (2016).

[106] T. Liu, K. Surapaneni, M. Lou, L. Cheng, P. Spincemaille, and Y. Wang, "Cerebral microbleeds: burden assessment by using quantitative susceptibility mapping," *Radiology* **262**, 269–278 (2012).

[107] A. Michelson, *Studies in optics* (Courier Corporation, 1995).

[108] S. Klein, M. Staring, K. Murphy, M. Viergever, and J. Pluim, "Elastix: a toolbox for intensity-based medical image registration," *IEEE Transactions on Medical Imaging* **29**, 196–205 (2010).

[109] P. Geladi and B. R. Kowalski, "Partial least-squares regression: a tutorial," *Analytica chimica acta* **185**, 1–17 (1986).

[110] R. Barnes, M. S. Dhanoa, and S. J. Lister, "Standard normal variate transformation and de-trending of near-infrared diffuse reflectance spectra," *Applied spectroscopy* **43**, 772–777 (1989).

[111] C. Spearman, "The proof and measurement of association between two things.," (1961).

[112] H. B. Mann and D. R. Whitney, "On a test of whether one of two random variables is stochastically larger than the other," *The annals of mathematical statistics* 50–60 (1947).

[113] A. J. Bishara and J. B. Hittner, "Testing the significance of a correlation with nonnormal data: comparison of Pearson, Spearman, transformation, and re-sampling approaches.," *Psychological methods* **17**, 399 (2012).

[114] S. S. Wilk and S. Shapiro, "An analysis of variance test for normality (complete samples)," *Biometrika* **52**, 591–611 (1965).

[115] E. Oei, J. van Tiel, W. Robinson, and G. Gold, "Quantitative radiologic imaging techniques for articular cartilage composition: toward early diagnosis and development of disease-modifying therapeutics for osteoarthritis," *Arthritis care research* **66**, 1129–1141 (2014).

[116] K. W. Fishbein, Y. A. Gluzband, M. Kaku, H. Ambia-Sobhan, S. A. Shapses, M. Yamauchi, and R. G. Spencer, "Effects of formalin fixation and collagen cross-linking on T2 and magnetization transfer in bovine nasal cartilage," *Magnetic Resonance in Medicine: An Official Journal of the International Society for Magnetic Resonance in Medicine* **57**, 1000–1011 (2007).

[117] P.-C. Lin, D. A. Reiter, and R. G. Spencer, "Sensitivity and specificity of univariate MRI analysis of experimentally degraded cartilage," *Magnetic Resonance in Medicine: An Official Journal of the International Society for Magnetic Resonance in Medicine* **62**, 1311–1318 (2009).

[118] P.-C. Lin, D. A. Reiter, and R. G. Spencer, "Classification of degraded cartilage through multiparametric MRI analysis," *Journal of magnetic resonance* **201**, 61–71 (2009).

[119] A. Dimov, Z. Liu, P. Spincemaille, M. Prince, J. Du, and Y. Wang, "Bone quantitative susceptibility mapping using a chemical species–specific R2* signal model with ultrashort and conventional echo data," *Magnetic Resonance in Medicine* (2017).

OLLI NYKÄNEN

―――――――――

Current diagnostic imaging methods do not sensitively detect early changes due to osteoarthritis. In this thesis, quantitative susceptibility mapping (QSM) and ultrashort echo time imaging by SWIFT-sequence were studied. QSM was not very sensitive to the degeneration of cartilage, but could be combined with T2* relaxation time mapping for better diagnostic performance. The results also showed that a bright signal at the osteochondral junction seen with the SWIFT-sequence is located in the non-calcified articular cartilage, contrasting previous studies placing it in the calcified cartilage.

UNIVERSITY OF
EASTERN FINLAND

uef.fi